

Delayed outflows from black hole accretion tori following neutron star binary coalescence

Rodrigo Fernández¹ and Brian D. Metzger²

¹ *Institute for Advanced Study, Princeton, NJ 08540, USA.*

² *Department of Physics, Columbia University, New York, NY 10027, USA.*

Submitted to MNRAS

ABSTRACT

Expulsion of neutron-rich matter following the merger of neutron star (NS) binaries is crucial to the radioactively-powered electromagnetic counterparts of these events and to their relevance as sources of r -process nucleosynthesis. Here we explore the long-term (viscous) evolution of remnant black hole accretion disks formed in such mergers by means of two-dimensional, time-dependent hydrodynamical simulations. The evolution of the electron fraction due to charged-current weak interactions is included, and neutrino self-irradiation is modeled as a lightbulb that accounts for the disk geometry and moderate optical depth effects. Over several viscous times (~ 1 s), a fraction $\sim 10\%$ of the initial disk mass is ejected as a moderately neutron-rich wind ($Y_e \sim 0.2$) powered by viscous heating and nuclear recombination, with neutrino self-irradiation playing a sub-dominant role. Although the properties of the outflow vary in time and direction, their mean values in the heavy-element production region are relatively robust to variations in the initial conditions of the disk and the magnitude of its viscosity. The outflow is sufficiently neutron-rich that most of the ejecta forms heavy r -process elements with mass number $A \gtrsim 130$, thus representing a new astrophysical source of r -process nucleosynthesis, distinct from that produced in the dynamical ejecta. Due to its moderately high entropy, disk outflows contain a small residual fraction $\sim 1\%$ of helium, which could produce a unique spectroscopic signature.

Key words: accretion, accretion disks — dense matter — gravitational waves — hydrodynamics — neutrinos — nuclear reactions, nucleosynthesis, abundances

1 INTRODUCTION

Coalescing neutron star (NS) and stellar mass black hole (BH) binaries are among the most promising sources for detection with networks of ground-based gravitational wave (GW) observatories, including Advanced LIGO and Virgo (Abramovici et al. 1992; Acernese et al. 2009; Caron et al. 1999; Abadie et al. 2010, 2012). The GW signal provides information on the properties of the merging binary (e.g., Ajith et al. 2007; van der Sluys et al. 2008); a potential probe of the equation of state of dense matter (e.g., Faber et al. 2002; Shibata 2005; Read et al. 2009; Bauswein et al. 2012); and even a test of General Relativity itself (e.g. Cornish et al. 2011).

To maximize the scientific benefit of a GW detection, it is important to identify a coincident electromagnetic counterpart (e.g. Bloom et al. 2009, Metzger & Berger 2012, Nissanke et al. 2013, Bartos et al. 2012). The sky localization provided by initial Advanced LIGO/Virgo will be tens to hundreds of square degrees (e.g. Fairhurst 2009; Wen & Chen 2010; Nissanke et al. 2011), but a coincident

X-ray, optical, or radio signal could provide a much more accurate position, such that the host galaxy and redshift of the merger could be identified. Electromagnetic emission also indirectly probes the (magneto-)hydrodynamics of the merger and its aftermath.

The BH created from a NS-NS merger, following a metastable hypermassive NS phase, is typically surrounded by a thick torus of mass $\sim 10^{-3} - 0.1M_\odot$ (Ruffert & Janka 1999; Uryū et al. 2000; Rosswog & Liebendörfer 2003; Oechslin & Janka 2006; Chawla et al. 2010; Rezzolla et al. 2010; Hotokezaka et al. 2011). A torus also forms following a BH-NS merger if the binary mass ratio is sufficiently low that the NS is tidally disrupted outside the BH instead of being swallowed whole (e.g. Faber et al. 2006; Duez et al. 2010; Foucart et al. 2011; Stephens et al. 2011; Foucart et al. 2012; East et al. 2012). The short accretion timescale $t_{\text{visc}} \lesssim 1$ s, and large accretion rates $\dot{M} \gtrsim M_\odot \text{ s}^{-1}$, of such remnant tori motivate the current paradigm that NS-NS/NS-BH mergers are the central engines power-

ing short duration gamma-ray bursts (SGRBs) (Paczynski 1986; Eichler et al. 1989).

Despite being well-studied, SGRBs do not necessarily represent an ideal counterpart for most GW-detected mergers because SGRBs are difficult to localize on the sky and their observed rate is relatively low ($\lesssim 1 \text{ yr}^{-1}$) within the sensitivity range of Advanced LIGO/Virgo (Metzger & Berger 2012; Chen & Holz 2012). These drawbacks have motivated the study of more *isotropic* merger counterparts, such as supernova-like optical transients powered by the decay of radioactive elements synthesized in the merger ejecta (‘kilonovae’, Li & Paczyński 1998; Kulkarni 2005; Metzger et al. 2010). Merger simulations show that a modest quantity of highly neutron rich material (electron fraction $Y_e \lesssim 0.1$) is ejected by tidal forces during the merger (Lattimer & Schramm 1974; Rosswog et al. 1999; Rosswog 2005; Chawla et al. 2010; Stephens et al. 2011; East et al. 2012; Rosswog 2012; Rosswog et al. 2013; Bauswein et al. 2013), and recent nuclear reaction network calculations largely agree on the amount of radioactive heating provided by such decaying r -process elements (Metzger et al. 2010; Roberts et al. 2011; Goriely et al. 2011).

One large uncertainty, however, is the opacity of the ejecta, because current kilonova models predict a composition dominated by heavy r -process nuclei (atomic mass number $A \gtrsim 130$). Recent atomic structure calculations show that the opacity of material containing even a small quantity of Lanthanide elements ($A \sim 139 - 175$) could be orders of magnitude higher than that of Fe (Kasen et al. 2013). This implies that the predicted transient peaks on longer timescales – up to a \sim week – and at a lower luminosity and frequency – in the near infrared rather than optical (Barnes & Kasen 2013; Tanaka & Hotokezaka 2013) – than in original models that assumed opacity similar to Fe (e.g. Metzger et al. 2010, Piran et al. 2013). Given the sensitive dependence of the signal on the Lanthanide fraction, it is thus crucial to identify any diversity in the nucleosynthetic composition of the ejecta.

Another uncertainty is the mass of the ejecta M_{ej} . Although the quantity of matter expelled in dynamical ‘tidal tails’ from the merger can be large ($\gtrsim 10^{-2} M_{\odot}$) in some cases (e.g. eccentric mergers; East et al. 2012), it is often found to be significantly smaller ($\sim 10^{-4} - 10^{-3} M_{\odot}$; Hotokezaka et al. 2013).

Dynamical expulsion is not the only source of ejecta, however. Mass loss also occurs in outflows from the accretion disk over longer, viscous timescales. Initially, neutrinos radiated from the disk – or from the central hyper-massive NS prior to its collapse – can heat and drive an outflow from the surface of the disk (a ‘neutrino-driven’ wind; e.g. McLaughlin & Surman 2005; Metzger et al. 2008; Surman et al. 2008; Dessart et al. 2009; Kizivat et al. 2010; Wanajo & Janka 2012). A potentially even larger quantity of mass is lost from the disk at later times due to powerful outflows driven by viscous heating and recombination of free nuclei into α -particles (Lee & Ramirez-Ruiz 2007; Beloborodov 2008; Metzger et al. 2008, 2009a; Lee et al. 2009).

Metzger et al. (2009a, hereafter MPQ09) constructed a height-integrated, time-dependent model of the viscous spreading of accretion disks formed from NS-NS/NS-BH mergers, including the evolution of the midplane electron

fraction Y_e due to weak interactions. MPQ09 find that as the disk spreads due to angular momentum transport and the temperature decreases, e^-/e^+ captures become slow compared to the viscous evolution timescale. Since these captures both cool the disk and affect its composition, the disk becomes geometrically thick and Y_e freezes out. Soon after freeze-out, free neutrons and protons recombine into α particles, starting near the outer edge of the disk and moving inwards with time. MPQ09 estimated that $\sim 20 - 50\%$ of the initial disk mass is unbound by this energy deposition, with a range of electron fractions $Y_e \sim 0.1 - 0.4$ resulting from varying local conditions during freeze-out (see also Lee & Ramirez-Ruiz 2007; Beloborodov 2008).

Lee et al. (2009) performed axisymmetric (2D) global simulations of long term disk evolution, which confirmed this process of He ‘evaporation’ explicitly. However, since they assumed β -equilibrium instead of explicitly following the weak interactions, they could not accurately determine the energy released by α -recombination or the electron fraction of the final ejecta. The electron fraction of disk outflows is critically important because it controls whether the heavy elements synthesized in the outflow are dominated by 2nd/3rd peak r -process elements (if $Y_e \lesssim 0.3 - 0.4$); lighter neutron-rich elements (if $0.3 - 0.4 \lesssim Y_e \lesssim 0.495$); or significant quantities of ^{56}Ni ($Y_e \gtrsim 0.495$) (e.g. Hoffman et al. 1997). Given the potentially large difference in the optical opacity of Fe-group and r -process elements, and the different geometry of tidal tails and disk winds, the resulting kilonova light curve, including contributions from both sources of ejecta, could in principle be much more complex than previously anticipated (Barnes & Kasen 2013; Tanaka & Hotokezaka 2013).

Beyond their implication for electromagnetic emission, disk outflows from binary NS mergers also represent an essentially unexplored astrophysical site for heavy element synthesis. This issue is particularly important because the astrophysical origin of r -process nuclei remains a mystery (Qian & Wasserburg 2007), and binary NS mergers could be an important – and possibly dominant – source (Lattimer & Schramm 1974; Freiburghaus et al. 1999; Korobkin et al. 2012). Nevertheless, with the exception of neutrino-driven disk outflows (e.g. Surman et al. 2008; Wanajo & Janka 2012), to date most studies of the r -process in such environments focus on the dynamical ejecta.

In this series of papers, we explore the long term evolution of the accretion disks formed by NS-NS/NS-BH mergers by means of axisymmetric (2D) time-dependent hydrodynamic simulations. In paper I (this work) we explore the dynamics of the disk evolution and the properties of the resulting disk outflows. In separate works, our results for the disk outflows will be used to make predictions for the resulting transient electromagnetic signature and nucleosynthetic yields.

Our models employ a finite-volume hydrodynamic method, a realistic equation of state, and a complete implementation of charged-current weak interactions in the optically-thin regime. Approximations are made in order to capture the key physical processes at a low computational cost: (1) the effects of general relativity on the disk dynamics are approximated via a pseudo-Newtonian potential, (2) neutrino self-irradiation is modeled as a ‘lightbulb’ that accounts for the basic disk geometry and includes cor-

rections for moderate optical depth effects, and (3) angular momentum transport is approximated by an anomalous shear-stress tensor with an α -viscosity. These approximations enable us to evolve accretion disks for a large number of orbits (~ 1000) and thus perform a parameter space study on the outflow properties which can guide future, more detailed calculations.

The paper is organized as follows. In §2 we briefly summarize the properties of the initial accretion disk. The numerical implementation is described in §3. Results are presented in §4, followed by a discussion in §5. Our conclusions are summarized in §6. The appendices provide additional information on the neutrino treatment as well as general information on accretion regimes and nucleosynthesis in NS merger disks.

2 DISK PROPERTIES

The mass of the torus formed during a NS-NS merger can vary considerably, $M_t \sim 10^{-3} - 0.1M_\odot$, depending on the binary mass ratio, the assumed EOS, the eccentricity of the initial orbit, and whether the system undergoes a long-lived hypermassive NS phase prior to BH formation (see Faber & Rasio 2012 for a recent review). The disk mass in a NS-BH merger also depends on the spin of the black hole, since spin controls the location of the innermost circular orbit. If the NS is tidally disrupted outside the BH horizon, then the torus mass is relatively large $M_t \sim 0.1M_\odot$; otherwise, the NS is swallowed whole and little or no torus forms (e.g., Foucart 2012). Merger simulations find that the initial torus is distributed across a wide range of radii, with most of the mass and angular momentum concentrated on a radial scale $R_0 \sim 20 - 100$ km.

The (Newtonian) orbital time at this radial scale is

$$t_{\text{orb}} = 3.5 \times 10^{-3} \left(\frac{R_0}{50 \text{ km}} \right)^{3/2} \left(\frac{M_{\text{BH}}}{3M_\odot} \right)^{-1/2} \text{ s}, \quad (1)$$

where M_{BH} is the BH mass. The characteristic timescale for matter to accrete may be estimated by the viscous time

$$\begin{aligned} t_{\text{visc}} &\simeq \alpha^{-1} \left(\frac{R_0^3}{GM_{\text{BH}}} \right)^{1/2} \left(\frac{H_0}{R_0} \right)^{-2} \\ &\sim 1 \text{ s} \left(\frac{0.03}{\alpha} \right) \left(\frac{R_0}{50 \text{ km}} \right)^{3/2} \left(\frac{3M_\odot}{M_{\text{BH}}} \right)^{1/2} \left(\frac{H_0}{3R_0} \right)^2, \end{aligned} \quad (2)$$

where H_0 is the vertical scaleheight and α parametrizes the disk viscosity (§3.3), resulting in a characteristic accretion rate

$$\begin{aligned} \dot{M}_0 &\sim \frac{M_t}{t_{\text{visc}}} \\ &\sim 10^{-2} M_\odot \text{ s}^{-1} \left(\frac{\alpha}{0.03} \right) \left(\frac{M_t}{10^{-2} M_\odot} \right) \left(\frac{R_0}{50 \text{ km}} \right)^{-3/2} \\ &\quad \times \left(\frac{M_{\text{BH}}}{3M_\odot} \right)^{1/2} \left(\frac{3H_0}{R_0} \right)^2. \end{aligned} \quad (3)$$

Due to the high densities and rapid evolution of the disk, photons are not an important source of cooling on timescales of relevance. However, the temperature is sufficiently high that neutrinos are relevant, especially in the earliest phases of the disk evolution (e.g.,

Popham et al. 1999; Narayan et al. 2001; Di Matteo et al. 2002; Chen & Beloborodov 2007; hereafter CB07). A straightforward calculation shows that a thin neutrino-cooled disk ($H \sim 0.1 - 0.3R_0$) obtains when the accretion rate at radius R_0 exceeds a critical value \dot{M}_ν given by (see Metzger et al. 2008, their eq. [11])

$$\dot{M}_\nu \approx 1.3 \times 10^{-2} M_\odot \text{ s}^{-1} \left(\frac{R_0}{50 \text{ km}} \right)^{5/6} \left(\frac{\alpha}{0.03} \right)^{5/3} \left(\frac{M_{\text{BH}}}{3M_\odot} \right)^{1/2}, \quad (4)$$

where the dominant source of cooling is assumed to be charged-current weak interactions, and general relativistic corrections have been neglected. Unlike photon-cooled disks, such as those in X-ray binaries or AGN, neutrino-cooled disks are the most radiatively efficient at small radii.

By equating R_0 in equation (4) with the radius R_{isco} of the innermost stable circular orbit of the BH, one obtains a critical accretion rate \dot{M}_{ign} (the ‘ignition’ rate) above which the disk is thin near its innermost radii:

$$\dot{M}_{\text{ign}} \approx 6 \times 10^{-2} [2 \times 10^{-2}] \left(\frac{\alpha}{0.03} \right)^{5/3} \left(\frac{M_{\text{BH}}}{3M_\odot} \right)^{4/3} M_\odot \text{ s}^{-1}, \quad (5)$$

where the prefactor was calculated by CB07 for a $3M_\odot$ black hole of spin $a = 0$ [$a = 0.95$] using a steady-state accretion model in a Kerr metric.

When the disk is neutrino-cooled ($\dot{M} > \dot{M}_\nu$) its internal energy e_{int} is dominated by non-degenerate nucleons (CB07). The characteristic temperature of the torus midplane, which is attained on a cooling timescale $t_{\text{cool}} \sim t_{\text{visc}}(H/R_0)^2$, is thus approximately given by

$$T_{\text{vir}} \simeq 7.6(1 + Y_e) \left(\frac{M_{\text{BH}}}{3M_\odot} \right) \left(\frac{3H_0}{R_0} \right)^2 \left(\frac{50 \text{ km}}{R_0} \right) \text{ MeV}, \quad (6)$$

where $Y_e = n_p/(n_n + n_p)$ is the electron fraction and n_p (n_n) are the number densities of protons (neutrons), respectively. The initial temperature of the disk is sufficiently high that all nuclei are dissociated into free nucleons. Alpha particles and heavier nuclei form only once the disk temperature decreases to $\lesssim 1$ MeV.

3 NUMERICAL SETUP

3.1 Equations Solved and Numerical Method

We solve the equations of mass, momentum, energy, and lepton number conservation on an axisymmetric spherical polar grid (r, θ) , with source terms due to gravity, shear viscosity, and optically-thin weak interactions

$$\frac{\partial \rho}{\partial t} + \nabla \cdot (\rho \mathbf{v}_p) = 0 \quad (7)$$

$$\frac{d\mathbf{v}_p}{dt} = \mathbf{f}_c - \frac{1}{\rho} \nabla p - \nabla \Phi \quad (8)$$

$$\rho \frac{d\ell_z}{dt} = r \sin \theta (\nabla \cdot \mathbb{T})_\phi \quad (9)$$

$$\rho \frac{de_{\text{int}}}{dt} + p \nabla \cdot \mathbf{v}_p = \frac{1}{\rho \nu} \mathbb{T} : \mathbb{T} + \rho \dot{Q}_{\text{net}} \quad (10)$$

$$\frac{dY_e}{dt} = \Gamma_{\text{net}}. \quad (11)$$

Here ρ , p , $\mathbf{v}_p = v_r \hat{r} + v_\theta \hat{\theta}$, and e_{int} denote the fluid density, pressure, poloidal velocity, and internal energy, respectively. The Lagrangian differential operator is $d/dt \equiv \partial/\partial t + \mathbf{v}_p \cdot \nabla$.

The specific angular momentum along the symmetry axis is given by $\ell_z = r \sin \theta v_\phi$, with v_ϕ the azimuthal velocity, and \mathbf{f}_c is the centrifugal force in the poloidal direction.

The pseudo-newtonian gravitational potential of Paczyński & Wiita (1980) is employed, $\Phi = -GM_{\text{BH}}/(r - R_S)$, with $R_S = 2GM_{\text{BH}}/c^2$ the Schwarzschild radius, as applicable to a BH of moderate spin.¹ The black hole mass is kept constant in the simulation. The neutrino source terms are \dot{Q}_{net} and Γ_{net} (see §3.2), and the viscous stress tensor is denoted by \mathbb{T} (see §3.3)

The *Helmholtz* EOS (Timmes & Swesty 2000) is used to relate internal energy and pressure. The ion component is an ideal gas of neutrons, protons, and alpha particles, with relative abundances that satisfy nuclear statistical equilibrium (NSE). Heavier nuclei are not included, since the energy release in their formation is much smaller in comparison, and hence should have little impact on the outflow dynamics². An additional (inert) hydrogen gas is used to populate the ambient medium that initially surrounds the torus. The zero point of energy is taken to be the pure nucleon state, with the internal energy becoming

$$e_{\text{int}} = e_{\text{int},0} - \frac{Q_\alpha}{m_\alpha} X_\alpha, \quad (12)$$

where $e_{\text{int},0}$ is the specific internal energy provided by the *Helmholtz* EOS, X_α is the mass fraction of alpha particles, m_α is the mass of an alpha particle, and $Q_\alpha \simeq 28.3$ MeV is the nuclear binding energy of an alpha particle (e.g., Audi et al. 2003). In addition, the thermodynamic derivatives of the pressure, internal energy, and entropy of the ions acquire terms that originate in the dependence of the ion abundances on temperature and density. If the temperature falls below 5×10^9 K, or if the mass fraction of inert hydrogen exceeds 1%, the abundances are frozen. Any hydrogen mixed with torus material is added to the proton mass fraction if the temperature is higher than 5×10^9 K.

We use FLASH3.2 (Dubey et al. 2009) to evolve the system of equations (7)-(11) with the dimensionally-split version of the Piecewise Parabolic Method (PPM, Colella & Woodward 1984). The public version of the code has been modified to allow for a non-uniformly spaced grid in spherical polar coordinates, as described in Fernández (2012).

The computational grid is logarithmically spaced in radius, covering the range $2R_S$ to $2 \times 10^3 R_S$ in most models. In the polar direction, the cell spacing is uniform in $\cos \theta$, covering the interval $[0, \pi]$. We adopt this grid structure because we intend to cover a large dynamic range in radius, and to concentrate the resolution near the midplane, given the quasi-spherical character of the outflows. Our standard resolution uses 64 cells per decade in radius and 56 cells in the polar direction, yielding approximately square cells at the midplane ($\Delta r/r \simeq \Delta \theta \simeq 2^\circ$). The coarsest angular cell next to the polar axis is 10.8° . One model is evolved at double the resolution in both radius and in angle, to quantify convergence.

The boundary conditions at the polar axis are reflecting

¹ BHs formed from NS-NS mergers have typical spin parameter $a \sim 0.7 - 0.8$ (e.g., Rezzolla et al. 2010)

² The formation of heavy nuclei would indeed occur at radii within our simulation grid, however, see §5.1

in all variables. At the inner and outer radial boundaries, we impose a zero-gradient boundary condition for all variables. In addition, the radial velocity in the ghost cells of the radial boundaries is set to zero if its value in the first active cell next to the boundary would imply mass entering the domain.

All energy and viscous source terms are set to zero when the density falls below a fiducial value of 10 g cm^{-3} . This value is sufficiently low as to not impact the outflows from the torus, yet sufficiently high to avoid requiring too small of a time step due to angular momentum transport in (unimportant) low-density regions.

To prevent numerical problems in the funnel that develops around the rotation axis, we impose a floor of density equal to 1 g cm^{-3} , and a floor of temperature at 10^5 K.

3.2 Neutrino Treatment

The inner regions of the disk become opaque to neutrinos above an accretion rate (Appendix A)

$$\dot{M}_{\text{opaque}} \simeq 0.15 M_\odot \text{ s}^{-1} \left(\frac{\alpha}{0.03} \right)^{4/5} \left(\frac{M}{3M_\odot} \right)^{7/10} \left(\frac{R_{\text{isco}}}{6R_g} \right)^{9/5}. \quad (13)$$

The condition $\dot{M}_{\text{opaque}} \gtrsim \dot{M}_0$ (eq. [3]), sets the minimum disk mass for optical thickness. For slowly spinning BHs, this mass is $\sim 0.1 M_\odot$.

Most of the disks we explore ($M_t \lesssim 0.1 M_\odot$) are thus only marginally optically thick to neutrinos at early times. Since the disk density decreases as accretion proceeds, full neutrino transparency is always achieved. The models we explore undergo this transition before weak freezeout occurs, as quantified by the magnitude of the optical depth, and hence we adopt an optically thin treatment of energy exchange with matter and regulation of the electron fraction in all cases. Finite optical depth corrections are included to prevent excessive heating at early times in the few massive tori we evolve.

Charged-current weak interactions are included as formulated by Bruenn (1985) and implemented by Fernández (2012). These reactions control the evolution of the electron fraction, and provide the dominant energy exchange channel between neutrinos and matter. The relevant source terms are the net rate of change of the electron fraction

$$\Gamma_{\text{net}} = \Gamma_{e-} - \Gamma_{e+}, \quad (14)$$

where Γ_{e-} and Γ_{e+} are the rates of electron and positron creation per baryon, respectively, and the net specific heating rate of the gas

$$\dot{Q}_{\text{net}} = \mathcal{H}_{\nu_e} + \mathcal{H}_{\bar{\nu}_e} - \mathcal{C}_{\nu_e} - \mathcal{C}_{\bar{\nu}_e} - \mathcal{C}_{\text{pairs}}, \quad (15)$$

where \mathcal{H}_{ν_e} and $\mathcal{H}_{\bar{\nu}_e}$ is the heating by absorption of neutrinos and antineutrinos on nucleons, respectively, and \mathcal{C}_{ν_e} and $\mathcal{C}_{\bar{\nu}_e}$ are the cooling rates from electron and positron capture, respectively. Explicit forms for these terms are provided in Appendix B. Additional neutrino energy losses from pair creation ($\mathcal{C}_{\text{pairs}}$) are included via the Itoh et al. (1996) parameterization.³ Source terms are included via explicit operator split in the equations for energy and lepton number conservation.

³ http://cococubed.asu.edu/code_pages/codes.shtml

Self-irradiation of the disk is implemented via a lightbulb-type prescription that accounts for the disk geometry (Appendix B). All of the neutrino emission is assumed to come from a ring of material on the midplane, with a radius R_{em} chosen to be an average value weighted by the neutrino emissivity,

$$R_{\text{em}} = \frac{\int \sin \theta \, d\theta \, dr \, r^3 \rho (\mathcal{C}_{\nu_e} + \mathcal{C}_{\bar{\nu}_e})}{\int \sin \theta \, d\theta \, dr \, r^2 \rho (\mathcal{C}_{\nu_e} + \mathcal{C}_{\bar{\nu}_e})}. \quad (16)$$

This approximation is justified by the highly peaked form of this emissivity (Appendix B), and the low optical depth of most of the disk masses considered. The neutrino luminosities of electron-type neutrinos L_{ν_e} and antineutrinos $L_{\bar{\nu}_e}$ used in this self-irradiation treatment are calculated at the end of the previous time step by integrating the corresponding emissivities over the whole torus. Spectra are assumed to follow a Fermi-Dirac distribution with zero chemical potential, with a temperature equal to the gas temperature in an angle-averaged radial shell (10% spread) around the emission radius R_{em} . Self-irradiation is included to explore its influence on the ejecta composition and its relative energetic contribution to the total mass loss. Results are not expected to be very sensitive to the particular choices of luminosities and spectra, because the process is energetically subdominant (e.g., Ruffert & Janka 1999, MPQ09).

To explore more massive tori, finite optical depth effects are approximated by a modified version of the Lee et al. (2004) treatment. At each time step, four optical depth functions for each neutrino species are computed from the neutrino emission peak,

$$\tau_i^{\text{up}}(\theta) = \int_0^\theta \kappa_i R_{\text{em}} d\theta', \quad \theta \in [0, \pi/2], r = R_{\text{em}} \quad (17)$$

$$\tau_i^{\text{dn}}(\theta) = \int_\theta^\pi \kappa_i R_{\text{em}} d\theta', \quad \theta \in [\pi/2, \pi], r = R_{\text{em}} \quad (18)$$

$$\tau_i^{\text{out}}(r) = \int_r^{r_{\text{out}}} \kappa_i dr', \quad r \in [R_{\text{em}}, r_{\text{out}}], \theta = \frac{\pi}{2} \quad (19)$$

$$\tau_i^{\text{in}}(r) = \int_{r_{\text{in}}}^r \kappa_i dr', \quad r \in [r_{\text{in}}, R_{\text{em}}], \theta = \frac{\pi}{2}, \quad (20)$$

corresponding to the four coordinate directions. Given that most of the torus mass lies within $\sim 45^\circ$ of the equator, we use angular integration to estimate the vertical optical depth. For fast computation, the absorption coefficients for this optical depth functions⁴ are approximated as in Janka (2001)

$$\kappa_{\nu_e} \simeq 2.2 \times 10^{-7} \rho_{10} T_{\nu_e,4}^2 \sqrt{X_p(2X_n + X_p)} \text{ cm}^{-1}, \quad (21)$$

$$\kappa_{\bar{\nu}_e} \simeq 2.2 \times 10^{-7} \rho_{10} T_{\nu_e,4}^2 \sqrt{X_p(2X_p + X_n)} \text{ cm}^{-1}. \quad (22)$$

The neutrino emissivities \mathcal{C}_{ν_e} and $\mathcal{C}_{\bar{\nu}_e}$ are then suppressed everywhere by a factor $\exp(-\tau_{i,\text{peak}})$, where

$$\tau_{i,\text{peak}} = \min[\tau_i^{\text{up}}(\pi/2), \tau_i^{\text{dn}}(\pi/2), \tau_i^{\text{out}}(R_{\text{em}}), \tau_i^{\text{in}}(R_{\text{em}})]. \quad (23)$$

This prescription accounts for the fact that most neutrinos will escape along the path with the least optical depth, which in most cases is the vertical direction. In contrast to Lee et al. (2004), we ignore the neutrino pressure contribu-

tion, which is a small correction (our tori are not radiation-dominated while optically thick).

The neutrino luminosity used for self-irradiation, first computed from the attenuated emissivities, is further suppressed by a local factor $\exp(-\tau_{i,\text{irr}})$, where

$$\tau_{i,\text{irr}}(r, \theta) = [\tau_i^x(R_{\text{em}}) - \tau_i^x(r)] + \frac{\tau_i^x(r)}{\tau_i^x(R_{\text{em}})} [\tau_i^y(\pi/2) - \tau_i^y(\theta)]. \quad (24)$$

The superscripts x and y are the radial and angular optical depths for the appropriate quadrant, respectively (eqns [17]-[20]). This prescription attempts to capture the attenuation of the neutrino flux in regions far from the emission peak, and smoothly approaches the semi-transparent lightbulb limit for decreasing torus density. It is a coarse approximation, however, since it does not account for attenuation along lateral directions, and assumes that the vertical density and abundance dependence differs only by a constant scaling factor at different radii.

In optically thick disks, the rate of change of the electron fraction (eq. [14]) is affected indirectly via the suppression of the self-irradiation luminosities. The portion due to the local neutrino emissivities is not modified, however, since its contribution will still vanish in beta equilibrium.

3.3 Angular Momentum Transport

Angular momentum transport is mediated by a viscous stress tensor \mathbb{T} for which only the azimuthal components are non-zero (e.g., Stone et al. 1999),

$$T_{r\phi} = \rho\nu \frac{r}{\sin\theta} \frac{\partial}{\partial r} \left(\frac{\ell_z}{r^2} \right) \quad (25)$$

$$T_{\theta\phi} = \rho\nu \frac{\sin\theta}{r^2} \frac{\partial}{\partial\theta} \left(\frac{\ell_z}{\sin^2\theta} \right). \quad (26)$$

Including all components of the stress would suppress convection in the poloidal direction (e.g., Igmenshchev & Abramowicz 1999). Our simulations mimic turbulent angular momentum transport via thermally-driven convection. Given the low mass of the torus relative to that of the central BH, and its relatively thick scaleheight, we consider our neglect of self gravity as a good approximation.

To connect with previous calculations, we employ a Shakura & Sunyaev (1973) parameterization of the kinematic viscosity coefficient

$$\begin{aligned} \nu_\alpha &= \alpha \frac{c_i^2}{\Omega_K} \\ &= \alpha \left(\frac{c_i^2}{GM_{\text{BH}}/r} \right) \sqrt{GM_{\text{BH}}R_0} \left(1 - \frac{R_S}{r} \right) \left(\frac{r}{R_0} \right)^{1/2} \end{aligned} \quad (27)$$

where Ω_K is the Keplerian frequency of the Paczyński & Wiita (1980) potential and $c_i^2 = p/\rho$ is the isothermal sound speed.

The implementation of angular momentum evolution in FLASH is described in Fernández & Metzger (2013). Viscous heating is handled as an explicit source term in the energy equation, while the diffusive momentum flux is added to the advective fluxes obtained during the Riemann solver step. Tests of this implementation are provided in Fernández & Metzger (2013).

⁴ Not to be confused with the absorption coefficients used in the actual neutrino absorption rates (Appendix B).

Table 1. Models Evolved and Outflow Properties. Columns from left to right are: initial torus mass, black hole mass, initial torus radius (eq. [28]), initial electron fraction, initial entropy, viscosity coefficient (eq. [27]), spatial resolution (std=standard, hi=high; §3.1), inclusion of recombination energy (eq. [12]), inclusion of self-irradiation (§3.2), mass-flux-weighted values of the electron fraction, entropy, and expansion time $t = r/\bar{v}_r$ at a radius where $\bar{T} \sim 5 \times 10^9$ K and within $\pm 60^\circ$ of the midplane (eq. [31]), ratio of the total mass with positive energy ejected beyond $r = 10^9$ cm to the total mass accreted through the ISCO radius, each in units of the initial torus mass, and mass-flux-weighted density (in units of 100 g cm^{-3}) and velocity (in units of $10,000 \text{ km s}^{-1}$) at $r = 10^9$ cm and within $\pm 60^\circ$ of the midplane.

Model	M_{t0}	M_{BH}	R_0	Y_{e0}	s_0	α	Res.	Rec.	Irr.	\bar{Y}_e	\bar{s}	t_{exp}	$M_{\text{ej}}/M_{\text{acc}}$	$\bar{\rho}_2$	$\bar{v}_{r,9}$
	(M_\odot)		(km)		(k_B/b)						(k_B/b)	(ms)	(M_{t0}/M_{t0})		
S-def	0.03	3	50	0.10	8	0.03	std	yes	yes	0.16	16	95	0.10/0.90	1.6	2.2
S-m0.01	0.01	3	50	0.10	8	0.03	std	yes	yes	0.15	18	68	0.10/0.90	0.5	2.2
S-m0.10	0.10									0.17	17	119	0.11/0.89	6.3	2.3
S-r75	0.03	3	75							0.16	16	126	0.22/0.78	3.6	2.2
S-M10		10	150							0.18	17	77	0.04/0.92	0.8	1.8
S-y0.05		3	50	0.05						0.15	16	93	0.10/0.90	1.5	2.2
S-y0.15				0.15						0.17	16	92	0.10/0.90	1.6	2.3
S-s6				0.10	6					0.14	17	86	0.08/0.91	1.2	1.9
S-s10					10					0.19	16	87	0.12/0.88	1.9	2.6
S-v0.01					8	0.01				0.20	18	193	0.11/0.89	1.5	2.5
S-v0.10						0.10				0.14	19	38	0.13/0.87	2.2	2.4
S-hr						0.03	hi			0.15	16	94	0.10/0.90	1.5	2.2
P-rec	0.03	3	50	0.10	8	0.03	std	no	yes	0.18	17	43	0.03/0.93	0.8	0.9
P-irr								yes	no	0.15	16	90	0.10/0.90	1.4	2.2
P-rec-irr								no	no	0.17	17	47	0.03/0.93	0.9	0.6
P-tau								yes	yes	0.21	17	76	0.13/0.87	2.1	2.7

3.4 Initial Conditions

The initial condition is an equilibrium torus with constant entropy, angular momentum, and electron fraction (e.g., Papaloizou & Pringle 1984; Hawley 2000). The initial solution is obtained by first finding the local density given the entropy, electron fraction, and position in the disk,

$$w(\rho, r, \theta) \Big|_{s, Y_e} = \frac{GM_{\text{BH}}}{R_0} \left[\frac{R_0}{r - R_S} - \frac{1}{2} \frac{R_0^2}{(r \sin \theta)^2} \left(\frac{R_0}{r - R_S} \right)^2 - \frac{1}{2d} \right], \quad (28)$$

where $w = e_{\text{int}} + p/\rho$ is the specific enthalpy of the fluid, and d is the torus distortion parameter. The resulting density distribution is then integrated to obtain the disk mass. The procedure is repeated, changing the entropy, until the desired torus mass is obtained. The distortion parameter d controls the thermal content of the solution; for fixed mass and electron fraction, it is uniquely determined by demanding a given entropy or a value of $H/R = c_i/(r\Omega_K)$ at the point of maximum density.

Evolving this equilibrium torus against a low-density background results in the emergence a shock from the edges of the disk due to strong gradients. To avoid confusing this initial transient with the viscously-driven outflow we are interested in, we evolve the initial torus for 100 orbital times at $r = R_0$ without angular momentum transport or energy source terms. At this time a power-law density profile has been established at large radii, and the total mass in torus material has decreased by a small amount ($< 1\%$), due to the spread to larger radii. The mass accretion rate at the ISCO due to numerical viscosity is $\sim 10^{-5} M_\odot \text{ s}^{-1}$. We then reset all positive radial velocities to zero and take this as the initial condition for the simulations.

A realistic merger will produce a torus with a more

general radial distribution of mass, angular momentum, and thermal energy, than we have assumed. However, we do not expect our results to be overly sensitive to the initial thermal distribution of the torus, since the temperature profile will equilibrate on a thermal timescale $t_{\text{cool}} \sim t_{\text{visc}}(H/R)^2 \sim 0.1t_{\text{visc}}$.

The torus is surrounded by an ambient medium of constant density with a value $\sim 20\%$ higher than the floor of density (§3.1), and pressure distribution $p_{\text{amb}} = -\Phi\rho_{\text{amb}}$ (Stone et al. 1999). The magnitude of the ambient density is chosen as the lowest value that does not cause numerical problems in the inner regions of the polar funnel.

3.5 Models Evolved

We evolve a number of models that explore the effect of (1) varying fundamental parameters in the system, and (2) artificially removing critical processes for outflow generation. All models are shown in Table 1.

The *S*-series of models include all the physics, and vary parameters around a fiducial model with $M_{\text{BH}} = 3M_\odot$, $\alpha = 0.03$, $M_t = 0.03M_\odot$, $Y_e = 0.1$, and $s = 8 k_B$ per baryon, with standard resolution (§3.1). We call this model S-def, and it is intended to roughly match the parameters of model B10 PaWi of Ruffert & Janka (1999, cf. their Figure 14). This model is also marginally optically thick to neutrinos at early times, becoming transparent (as measured by the minimum optical depth τ_{peak} [eq. 23]) after 5 orbits at $r = R_0$. Models in this series explore the effect on the outflows of varying the torus mass (S-m0.01, S-m0.10), torus radius (S-r75), black hole mass (S-M10), initial electron fraction (S-y0.05 and S-y0.150), initial entropy (S-s6 and S-s10), magnitude of the viscous stress tensor (S-v0.01 and S-0.10), and resolution (S-hr). Models in this series are evolved for 1000 orbits at

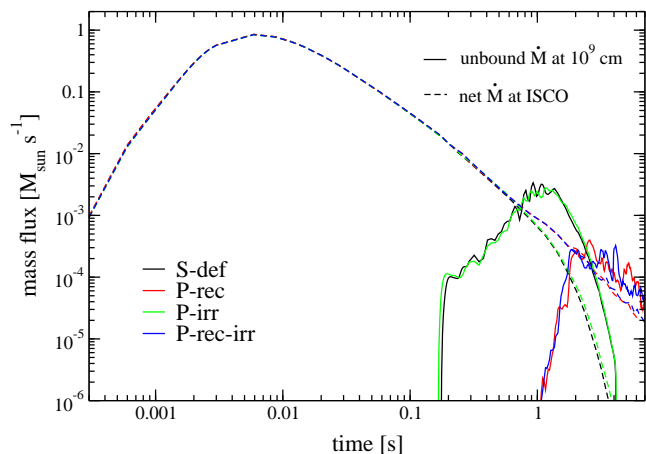


Figure 1. Angle-integrated mass outflow rate in unbound material at $r = 10^9$ cm (solid lines) and net mass accretion rate at the ISCO (dashed lines) as a function of time for model S-def (black). Also shown are models that suppress the nuclear binding energy of alpha particles (P-rec, red), self-irradiation (P-irr, green), or both (P-rec-irr, blue). The orbital time at $r = R_0$ is 2.9 ms.

$r = R_0$, except S-def, which is evolved for 3000 orbits at the same location.

The *P*-series explores the effect of suppressing physical processes relative to model S-def, to study the effect on the outflow generation. In model P-rec, we remove the binding energy of alpha particles by setting $Q_\alpha = 0$ in equation (12) in both the initial condition and the subsequent evolution. The series also explores the effect of shutting down self-irradiation (P-irr), as well as the effect of suppressing both recombination and self-irradiation simultaneously (P-rec-irr). We also test the effect of the optical depth corrections to self-irradiation, by setting $\tau_{i,\text{irr}} = 0$ (eq. [24]) in model P-tau (the global suppression of neutrino emission by τ_{peak} [eq. 23] is still included). All models in this series are evolved for 3000 orbits at $r = R_0$.

4 RESULTS

4.1 Outflow generation

All tori undergo the same basic evolutionary stages. The disk spreads in radius due to angular momentum transport, and the internal energy is modified by viscous heating, nuclear recombination, and neutrino source terms. The accretion rate at the ISCO reaches a peak magnitude at time $\sim 0.1/\alpha$ orbits at $r = R_0$, later decaying as a power-law in time after $\sim 1/\alpha$ orbits at the same location (Figure 1).

The inner regions of the disk are initially sufficiently hot for neutrino cooling to balance viscous heating. In contrast, the outer regions are colder, and viscous heating dominates over neutrino cooling (e.g., MPQ09). This net heating, combined with the transport of angular momentum to larger radii, causes an expansion in the outer regions of the disk as shown in Figure 2 for model S-def. The outermost regions achieve positive specific energy

$$e_{\text{tot}} = \frac{1}{2}v_p^2 + \frac{1}{2} \frac{\ell_z^2}{(r \sin \theta)^2} + e_{\text{int}} + \Phi \quad (29)$$

and are therefore unbound from the central BH.

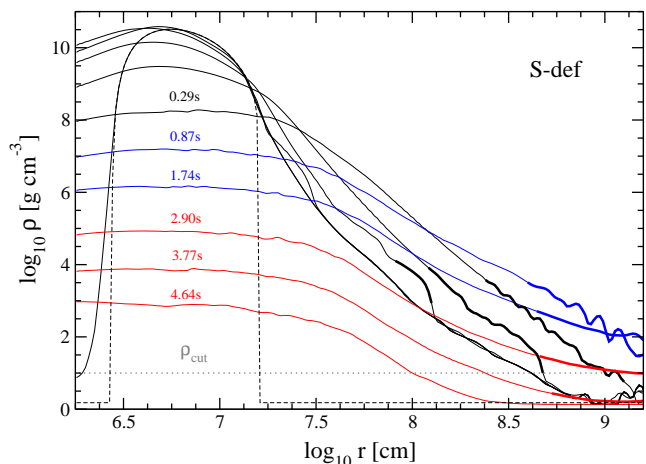


Figure 2. Evolution of the angle-averaged density in model S-def, illustrating the generation of the outflow. Curves correspond to times chosen in multiples of the orbital time at $r = R_0$ (2.9 ms), showing 0, 3, 10, 30, 100, 300, 600, 1000, 1300, 1600 orbits, as labeled. The bold curve segments correspond to material that has positive energy (eq. [29]). The horizontal dotted line marks the density at which source terms are suppressed for numerical reasons, and the dashed line shows the equilibrium torus before relaxation for the initial condition (§3.4).

The mass outflow rate in unbound material at $r = 10^9$ cm for model S-def is shown in Figure 1. It rises from low values to a peak at ~ 1 s or (~ 400 orbits at $r = R_0$) that exceeds the magnitude of the mass loss at the ISCO. This outflow is much denser than that generated by the initial expansion of the equilibrium torus in the low-density ambient medium, and which generates the background power-law density profile (Figure 2).

The relative contribution of viscous heating, nuclear recombination, and self-irradiation to the outflow generation is examined in Figure 1. The mass accretion rate and outflow rate of the default model S-def is compared with those from models that suppress the nuclear recombination energy (P-rec), self-irradiation (P-irr), and both nuclear energy and self-irradiation simultaneously (P-rec-irr). The recombination of alpha particles has the strongest effect on the disk evolution, by (1) causing a more energetic and massive outflow to arise earlier, and (2) by strongly suppressing the mass accretion rate at the ISCO. This drop in the accretion rate at late times is consistent with the results of Lee et al. (2009).

Self-irradiation has only a minor effect on the energetics of the system. In model S-def, neutrino heating is always smaller than viscous heating by at least a factor of several. This sub-dominance of self-irradiation can be traced to a few causes: (1) the neutrino luminosities are high only for a limited period of time, because both the mass and the temperature of the torus decrease with time, as shown in Figure 3 for model S-def; (2) self-irradiation is the strongest at the time where the torus becomes optically thin, and affects mostly vertical, low-density regions of the inner disk; and (3) the temperature in the emission region decreases with time (Fig. 3), resulting in lower mean energies of the neutrinos and thus a decreasing energy deposition rate. For illustration, a snapshot of the ratio of neutrino heating to

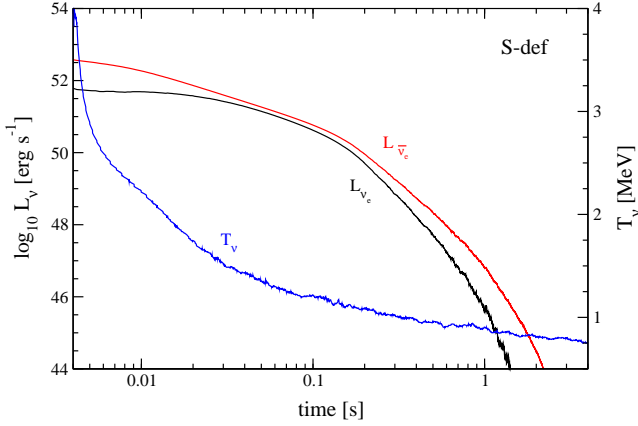


Figure 3. Time evolution of the neutrino and antineutrino luminosities (black and red, respectively) and neutrino temperature (blue) for model S-def.

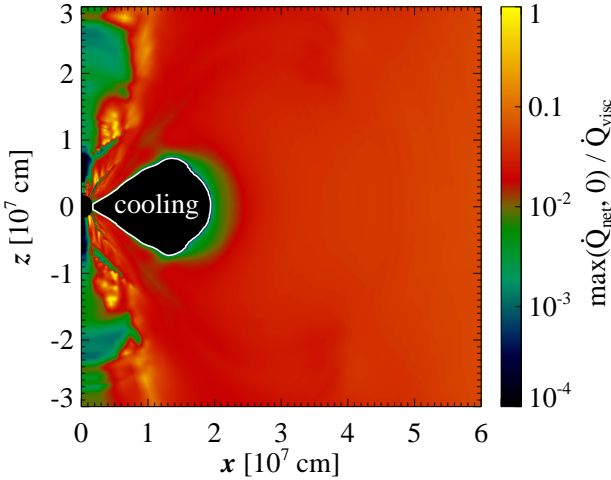


Figure 4. Ratio of neutrino heating to viscous heating $\dot{Q}_{\text{net}} = T : \mathbb{T} / (\nu \rho^2)$ (eq. [10]) in model S-def-hr at time 0.058s (orbit 20 at $r = R_0$). The white contour shows the surface $\dot{Q}_{\text{net}} = 0$, inside which neutrino cooling dominates.

viscous heating in model S-def-hr is shown in Figure 4. The effect is not entirely negligible however, as turning off optical depth corrections leads to $\sim 20\%$ changes in the electron fraction and the asymptotic velocity (§4.2).

The total mass accreted through the ISCO radius and the mass with $e_{\text{tot}} > 0$ ejected beyond a radius of 10^9 cm are given in Table 1 as fractions of the initial torus mass. In most models, approximately 10 per cent of the torus mass is ejected, with the rest accreting onto the BH. One exception is the model S-r75 with a larger initial torus radius, which ejects twice as much mass as the default model. Another exception is model S-M10, which while having a large disk radius, also has a higher BH mass, which leads to smaller mass ejection by $\sim 50\%$. The other two outliers are the models that suppress nuclear recombination (P-rec and P-rec-irr), for which ~ 3 per cent of the mass is ejected (c.f. Figure 1). Doubling the resolution in each coordinate direction leads to insignificant quantitative differences, so we consider our results converged. Given the range of disk masses explored,

the ejecta mass from delayed outflows can thus range from 10^{-3} to $10^{-2} M_{\odot}$.

The morphology of the ejecta is quasi-spherical, with most of the material being ejected within $\sim 60^\circ$ of the disk midplane, as shown in Figure 5. The bulk of the disk has moderate entropy (~ 20), particularly in regions relevant for nucleosynthesis (§4.2). At large radii ($\sim 10^9$ cm), the outflowing material develops shocks that raise its entropy. Large scale instabilities are also seeded by convection in the disk, which cannot cool efficiently once its accretion rate falls below \dot{M}_{ign} (eq. [5]). The funnel within a few tens of degrees from the polar axis has different properties; we do not study them here given our very approximate treatment of general relativity, and our omission of energy deposition by neutrino pair annihilation.

4.2 Outflow properties

At early times and in the innermost regions of the disk ($r \lesssim 100$ km), weak interactions are faster than the viscous time, and the electron fraction reaches its equilibrium value given the local density and temperature (e.g., Beloborodov 2003). As the disk evolves, the temperature and density decrease to the point that weak interactions operate slower than the viscous time and the electron fraction freezes out, becoming an advected quantity only (MPQ09). This process is illustrated for our fiducial model in Figure 6.

In the inner regions of the disk, the equilibrium electron fraction is initially small because electrons are more abundant than positrons when the disk is degenerate. However, with time Y_e rises to a maximum value ~ 0.3 because the disk becomes less degenerate as the density decreases. Most of this high- Y_e material is accreted onto the BH, however. The outer parts of the disk that eventually become unbound never achieve such high electron fractions and are instead ejected with $Y_e \lesssim 0.2$.

At a given radius, the wind material is not homogeneous in composition, but instead shows some variation around mean values. Figure 7 shows mass-flux weighted quantities crossing a spherical surface at the fixed radius $R_{\text{out}} = 10^9$ cm in the models S-def and P-irr. Quantities are computed according to

$$\langle A(R_{\text{out}}, t) \rangle = \frac{\int_{\theta_{\text{min}}}^{\theta_{\text{max}}} \sin \theta d\theta R_{\text{out}}^2 \rho v_r A(R_{\text{out}}, \theta, t)}{\int_{\theta_{\text{min}}}^{\theta_{\text{max}}} \sin \theta d\theta R_{\text{out}}^2 \rho v_r}, \quad (30)$$

where $A(R_{\text{out}}, \theta, t)$ is a generic scalar quantity, and $[\theta_{\text{min}}, \theta_{\text{max}}]$ is the angular range of the meridional integral, chosen as a wedge within 60° of the midplane (c.f. Figure 5). The bulk of the ejected material has $Y_e \sim 0.2$ and velocities $v_r \sim 20,000$ km s^{-1} .

Heavy nuclei generation occurs in regions where $T \sim 5 \times 10^9$ K (Hoffman et al. 1997). In the fiducial model S-def, this corresponds to a range of radii 200–400 km on the midplane depending on the phase in the disk evolution. To quantify the thermodynamic properties relevant for nucleosynthesis in the disk, we compute time- and angle-integrated mass-weighted mean values

$$\bar{A}(R_{\text{nuc}}) = \frac{\int dt \int \sin \theta d\theta R_{\text{nuc}}^2 \rho v_r A(R_{\text{nuc}}, \theta, t)}{\int dt \int \sin \theta d\theta R_{\text{nuc}}^2 \rho v_r}, \quad (31)$$

where the radius R_{nuc} is chosen so that $\bar{T} \simeq 5 \times 10^9$ K. The

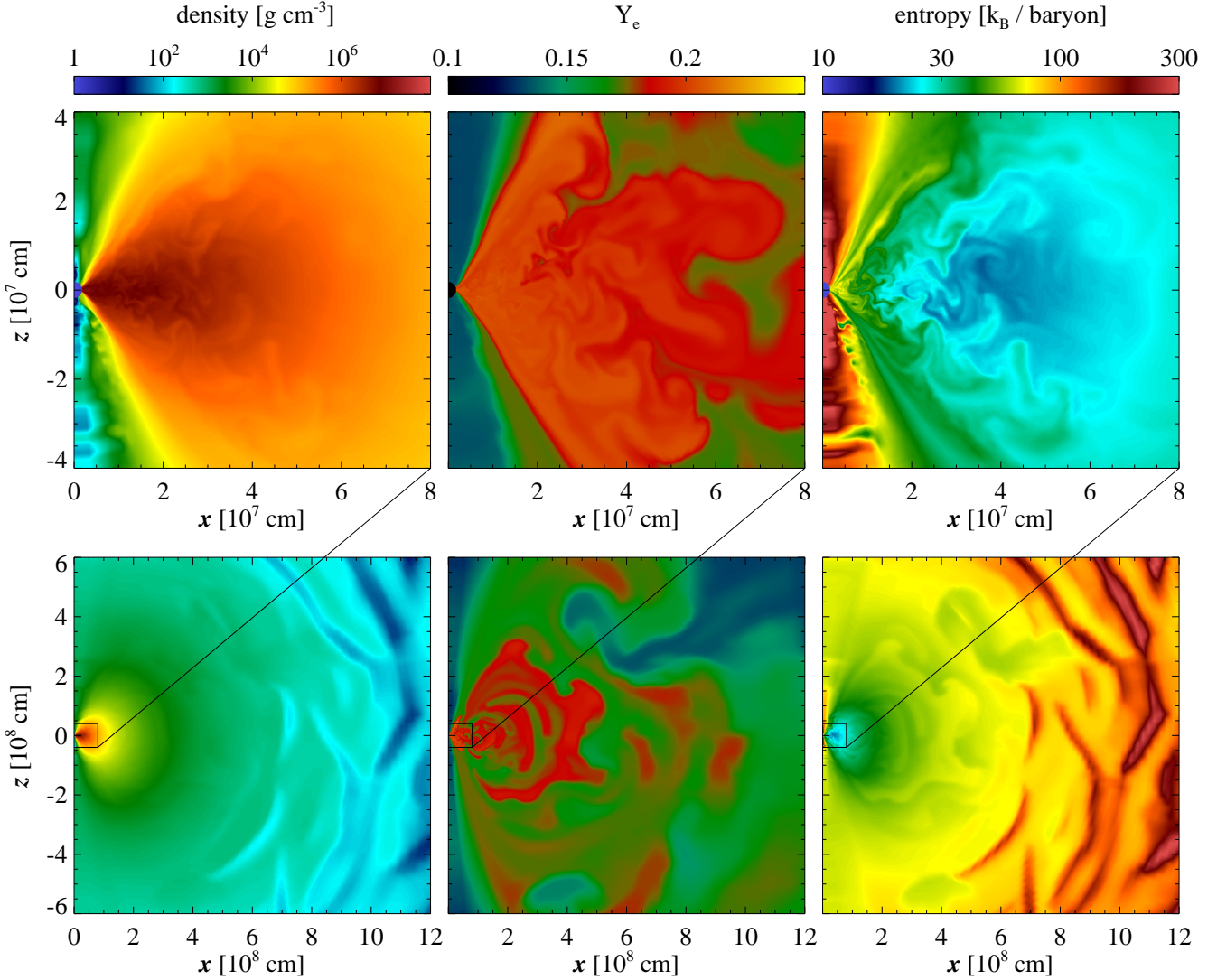


Figure 5. Color maps of density (left), electron fraction (middle), and entropy (right) in model S-def-hr at time 1.16s (orbit 400 at $r = R_0$), illustrating the wind morphology. Upper panels show zoomed in regions of the panels directly below, as indicated by the boxes. An animated version of this figure is available in the online journal.

resulting mean values of the electron fraction, entropy, and expansion time at R_{nuc} (within 60° of the midplane) are shown for all models in Table 1.

The composition is largely insensitive to variations in the model parameters, with typical mean values $\bar{Y}_e \sim 0.2$, $\bar{S} \sim 20k_B$ per baryon, and expansion timescales $t_{\text{exp}} = R_{\text{nuc}}/\bar{v}_r \sim 0.1$ s. The magnitude of the spread from the mean value is illustrated in Figure 8, which breaks up the mean values of Y_e , entropy, and expansion time for model S-def.

The value of \bar{Y}_e is relatively insensitive to the initial electron fraction because most of the disk mass achieves weak equilibrium, erasing its initial composition. The largest difference in \bar{Y}_e occurs due to changes in the initial entropy of the disk and the magnitude of the viscosity. The entropy of the torus is related to the level of degeneracy, which in turn determines the value of the equilibrium electron fraction (e.g., Beloborodov 2003). The magnitude of the viscosity determines the ratio of the weak equilibration time t_{weak}

to the viscous times t_{visc} . A smaller viscosity implies that these two timescales become equal at a large radius, which increases the amount of processed Y_e that enters the outflow. This modest dependence of Y_e on α is, however, mitigated by two facts: (1) the disk is regulated by neutrino cooling to moderate degeneracy (CB07), independent of the magnitude of viscous heating; (2) the disk becomes radiatively inefficient (and hence thicker and less degenerate) on the same timescale that Y_e freezes out. This coincidence results from the fact that e^-/e^+ captures both cool the disk and change Y_e (Metzger et al. 2009a).

The effects of self-irradiation on the ejecta composition are illustrated by Figure 7, which compares the polar mass-flux weighted composition for model S-def, P-irr (which suppresses self-irradiation), and P-tau (which turns off optical depth corrections to self-irradiation). Including self-irradiation with optical depth correction leads to a nearly identical outcome than suppressing irradiation altogether. As with the small energetic relevance of neutrino heating,

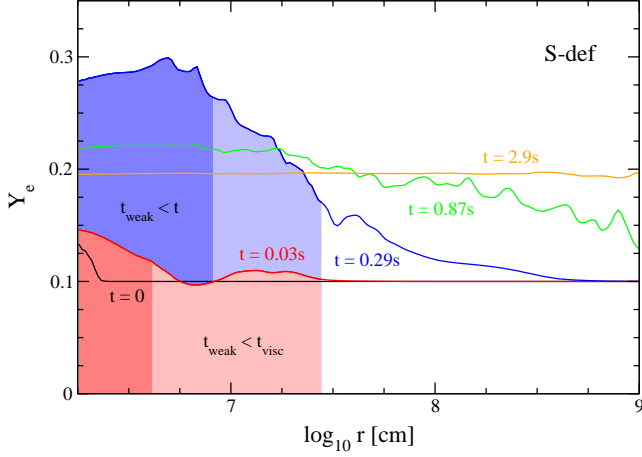


Figure 6. Angle-averaged, mass-weighted electron fraction at selected times for model S-def, as labeled. The dark-filled region corresponds to the weak equilibration time $t_{\text{weak}} = Y_e/|\Gamma_{\text{net}}|$ being smaller than the curve time, while the light-filled region is such that t_{weak} is shorter than the viscous time t_{visc} .

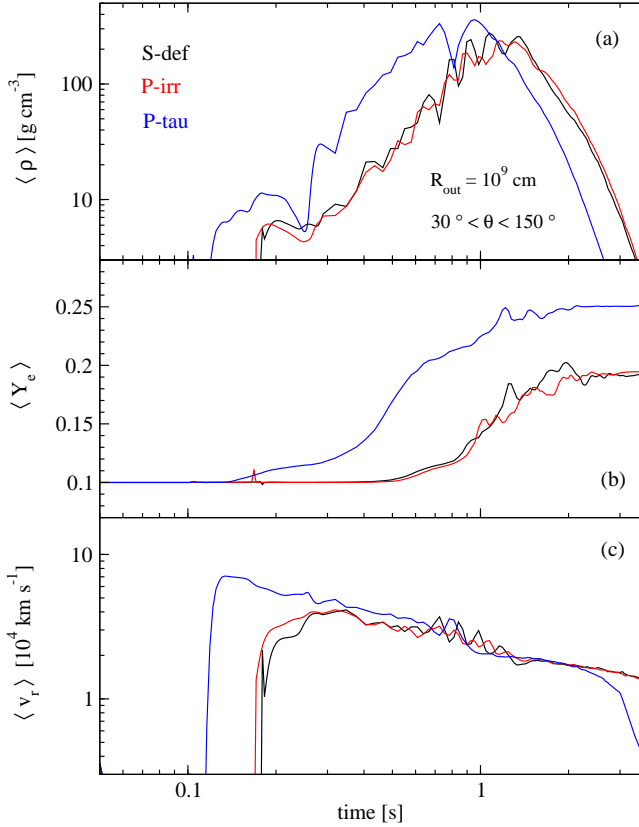


Figure 7. Instantaneous mass-flux-weighted quantities at a radius $R_{\text{out}} = 10^9$ cm for models S-def, P-irr (no self-irradiation), and P-tau (no optical depth suppression). Shown are the density ρ (a), electron fraction Y_e (b), and velocity v_r (c). The average is conducted over polar angles within 60° of the equator.

changes in the composition due to neutrino irradiation are important only around the time when the disk becomes transparent to neutrinos and its luminosity is still high. This timescale of peak irradiation is somewhat shorter than that required to significantly change the composition by weak interactions. The largest possible effect of neutrino heating on the outflow is probed by model P-tau, which completely suppresses optical depth corrections to the self-irradiation luminosity (while still globally suppressing the cooling rates). The outflow begins earlier, achieves asymptotic velocities that are $\sim 20\%$ larger, and has a mean Y_e that is 0.05 larger than the default model. Such moderate changes given an unrealistically large neutrino absorption rate reaffirms our conclusion that self-irradiation is only a small correction to the overall dynamics for low mass disks.

The expansion velocity at larger radii is remarkably constant, sensitive only to the inclusion of the nuclear binding energy of alpha particles. Note however that these values likely underestimate the true expansion velocities by a factor $\sim 1.4 - 1.7$ since we do not include the additional energy of \sim few MeV nucleon $^{-1}$ released in forming seed particles and (on somewhat longer timescales ~ 1 s) heavy r -process nuclei.

5 DISCUSSION

5.1 Nucleosynthesis in Disk Outflows

Appendix C reviews the conditions for heavy element nucleosynthesis in hot outflows, such as those from NS merger accretion disks, and provides analytic formulae for the fraction of the ejected mass synthesized into heavy r -process nuclei X_h and the fraction $X_\alpha = 1 - X_h$ that remains in α -particles (eq. [C1]). Given the low electron fraction $Y_e \lesssim 0.2$ of the disk outflows found in our calculations, we conclude that most of the ejecta will go into 2nd and 3rd peak r -process elements with mass number $A \sim 130 - 200$ ($X_h \simeq 1$). A much smaller fraction, $X_{\text{He}} \sim 10^{-2}$, will remain in ^4He , which may have implications for the spectroscopic signatures of these events (§5.2).

The average Galactic production rate of r -process nuclei due to accretion disk outflows from binary NS mergers is given by

$$\begin{aligned} \dot{M}_r &= \mathcal{R}_{\text{NS}^2} f_{\text{ej}} \bar{M}_t \\ &= 10^{-7} M_\odot \text{yr}^{-1} \left(\frac{\mathcal{R}_{\text{NS}^2}}{10^{-4} \text{yr}^{-1}} \right) \left(\frac{f_{\text{ej}}}{0.1} \right) \left(\frac{\bar{M}_t}{10^{-2} M_\odot} \right), \end{aligned} \quad (32)$$

where $\mathcal{R}_{\text{NS}^2}$ is the rate of NS-NS mergers scaled to its estimated value in the Milky Way (uncertain by at least an order of magnitude; Kalogera et al. 2004), \bar{M}_t is the average mass of the initial accretion torus, and $f_{\text{ej}} \sim 0.1$ is the fraction of M_t ejected in outflows, scaled to the characteristic value derived from our numerical simulations. Equation (32) should be compared with the ‘observed’ rate $\dot{M}_r^{\text{obs}} \sim 5 \times 10^{-7} M_\odot \text{yr}^{-1}$ required to explain the abundances of heavy $A \gtrsim 130$ r -process elements produced over the age of the Galaxy (Qian 2000). This shows that NS merger disk outflows constitute a potentially significant r -process source.

Although the idea that NS mergers are a promising r -process source is not new (Lattimer & Schramm 1974), pre-

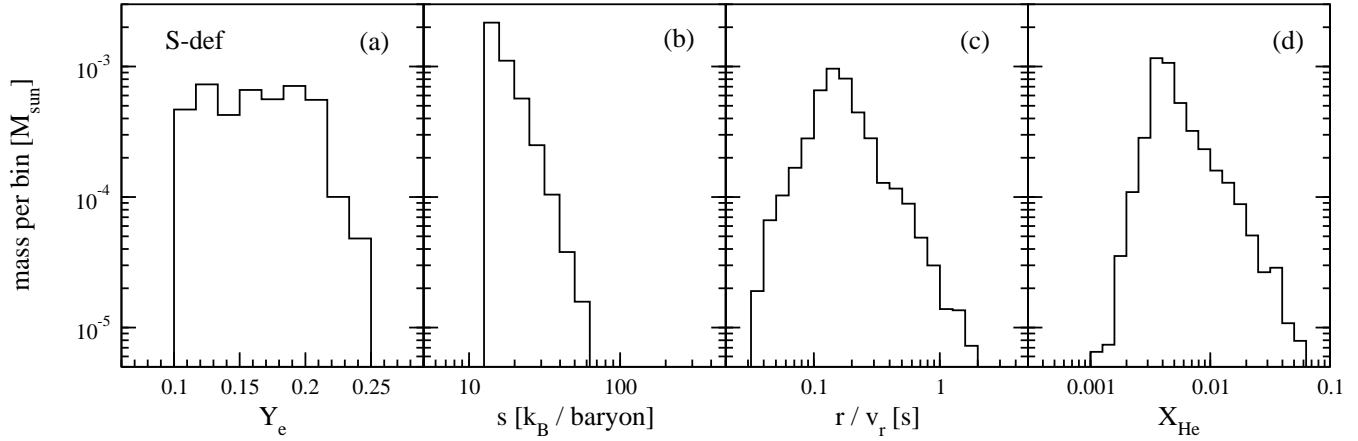


Figure 8. Thermodynamic properties of disk material for model S-def at a radius $R_{\text{nuc}} = 400$ km, where $\bar{T} \simeq 5 \times 10^9$ K. The histograms are constructed by considering all material that crosses this radius, within 60° of the midplane, over the entire disk evolution. Shown are the electron fraction Y_e (a), entropy S (b), expansion time $t_{\text{exp}} = r/v_r$ (c), and final helium mass fraction (d) computed from equation (C1).

vious studies have focused almost exclusively on nucleosynthesis of the dynamical ejecta.

Our simulations show no clear evidence for outflows powered primarily by neutrino heating. Such a wind was previously anticipated to dominate mass loss from small radii in the disk (e.g. Metzger et al. 2008; Surman et al. 2008; Wanajo & Janka 2012). Because neutrinos and antineutrinos from the disk have similar luminosities and mean energies, neutrino absorption is expected to drive Y_e to a value ~ 0.5 . Although our simulations do show unbound polar outflows, the electron fraction of this material is increased only slightly by neutrino irradiation (Fig. 7), since viscous heating dominates the unbinding of matter from the disk (Fig. 4). This hierarchy is contingent upon our assumption of an α -viscosity, which may not reflect the true vertical distribution of turbulent dissipation in the disk. Our approximate treatment of neutrino physics prevents us from definitively ruling out a strong role of self-irradiation. However, if an even larger fraction of the dissipation occurs in the disk corona in more realistic magnetized disks (e.g. Hirose et al. 2006), then the dominance of ‘viscous’-driven (low Y_e) polar outflows may turn out to be a robust feature of the launching mechanism. Regardless of the composition of the [possibly neutrino-driven] winds from small radii in the disk, the late outflows powered by α recombination and viscous heating almost certainly dominate the total (time-integrated) mass loss.

5.2 Radioactively-Powered Emission

Radioactive decay of r -process elements synthesized in the disk outflows gives rise to an electromagnetic transient similar to a dim supernova (e.g. Li & Paczyński 1998). Although the disk outflows are mildly anisotropic (Fig. 5), the ejecta will become increasingly spherical as it expands homologously with a characteristic velocity $\bar{v}_r \simeq 0.1c$ (Table 1). Most of the energy released by the r -process occurs on a timescale \sim seconds, but this heating is lost to adiabatic expansion since the outflow is highly optically thick at this early stage. Nevertheless, radioactive decay continues to add

energy to the ejecta, at an approximately constant rate per logarithmic time (e.g. Metzger et al. 2010). Electromagnetic emission peaks only once the timescale for photons to diffuse through the ejecta $t_d \propto \kappa M_{\text{ej}}/cr$ becomes shorter than the expansion timescale $t_{\text{exp}} = r/\bar{v}_r$. This occurs on a timescale (Metzger et al. 2010, eqs. [3],[4])

$$t_p \approx 7\text{d} \left(\frac{\bar{v}_r}{0.1c} \right)^{1/2} \left(\frac{M_{\text{ej}}}{10^{-2}M_\odot} \right)^{1/2} \left(\frac{\kappa}{10 \text{ cm}^2 \text{ g}^{-1}} \right)^{1/2} \quad (33)$$

resulting in emission with a characteristic peak luminosity

$$L_p \simeq 2.4 \times 10^{40} \text{ erg s}^{-1} \left(\frac{\bar{v}_r}{0.1c} \right)^{-1/2} \times \left(\frac{M_{\text{ej}}}{10^{-2}M_\odot} \right)^{1/2} \left(\frac{\kappa}{10 \text{ cm}^2 \text{ g}^{-1}} \right)^{-1/2}, \quad (34)$$

where κ is the opacity, scaled to a value characteristic of the line opacities of Lanthanide elements, given their expected abundance in the r -process ejecta (Kasen et al. 2013).

Because the composition of the disk outflows (predominantly heavy r -process nuclei) is similar to that of the dynamically ejected tidal tails, it may be observationally challenging to distinguish their contribution to the transient emission. One unique feature of the disk outflows, however, is the presence of a modest amount of helium ($X_{\text{He}} \sim 10^{-2}$), which is not present in the dynamical ejecta due to its much lower entropy $S \lesssim k_b \text{ baryon}^{-1}$ (since $X_{\text{He}} \propto S^{3/2}$; eq. [C1]).

Even a small quantity of He may be detectable if emission/absorption lines (e.g. He I $1.083\mu\text{m}$ and He I $2.058\mu\text{m}$) are produced as the result non-thermal excitation, induced by energetic γ -rays, β -decay electrons and fission products from decaying r -process elements. This is in analogy to the mechanism responsible for producing He lines in core-collapse SNe as the result of mixing radioactive ^{56}Ni into the outer layers of the ejecta (e.g. Lucy 1991, Dessart et al. 2012). Though a potentially promising diagnostic of conditions close to the merger site, future work is required to quantify the strength of He emission lines in kilonovae.

5.3 Effects of a Long-Lived Hypermassive NS

In the case of NS-NS mergers, our calculations implicitly assume that a BH forms within a few dynamical times after coalescence. If, however, the collapse is significantly delayed due to, e.g., thermal pressure and/or differential rotational support (Morrison et al. 2004; O’Connor & Ott 2011; Paschalidis et al. 2012; Lehner et al. 2012), then the effects of neutrino irradiation from the hyper-massive NS (HMNS) could qualitatively alter the properties of the disk evolution and its outflows.

To significantly alter the disk *dynamics*, neutrino emission from the HMNS would need to maintain both a high flux level, and a high mean neutrino energy, for a timescale longer than both (1) the time required to achieve neutrino transparency; and (2) the thermal time of the disk, such that the internal energy is raised sufficiently to unbind the disk. Such neutrino-driven outflows necessarily occur via thermal evaporation (e.g. McLaughlin & Surman 2005; Metzger et al. 2008; Surman et al. 2008; Dessart et al. 2009), as in the case of proto-neutron star winds, since momentum transfer from neutrinos is negligible.⁵

Even if neutrino irradiation from the HMNS is insufficient to alter the dynamics of the disk, it may still alter its composition, especially in outer parts of the disk where the rate of electron/positron captures is slow. To the extent that the HMNSs formed in binary NS merger are similar to the proto-neutron stars formed in core collapse supernovae, the neutrino and antineutrino luminosities and temperatures are expected to be similar. The net effect of HMNS irradiation on the disk would thus be to raise Y_e in both the disk midplane and in subsequent outflows (Dessart et al. 2009; see Metzger et al. 2009b and Darbha et al. 2010 for an analogous scenario following the accretion-induced collapse of a white dwarf). Spectroscopic or photometric signatures of elements synthesized exclusively in proton-rich ejecta of kilonovae (e.g., Fe or ^{56}Ni) could thus be taken as evidence for a long-lived HMNS. One significant difference between an r -process-rich and an Fe-rich outflow is the opacity of the ejecta, which drastically changes the rise time and peak luminosity of the light curve (Barnes & Kasen 2013; Tanaka & Hotokezaka 2013). Future work is necessary to quantify how long such a HMNS must survive in order to appreciably alter the outflow properties from the purely BH accretion scenario studied in this paper.

5.4 Comparison with Previous Work

Ruffert & Janka (1999) first studied the evolution of disks formed after NS coalescence in 3D using a realistic equation of state, a finite volume hydrodynamic method, Newtonian and pseudo-Newtonian potentials, and a neutrino leakage scheme (Ruffert et al. 1996). Follow up work by Setiawan et al. (2004) and Setiawan et al. (2006) explored the effect of including an α viscosity over a wide range of disk masses, finding that neutrino emission is sensitive to the magnitude of α . Our results cannot be directly compared to theirs, however, because their models were evolved only up

to 70 ms. Also, due to the equation of state used, their density floor was set at 10^8 g cm^{-3} , which would make it hard to develop any viscously driven outflow (c.f. Figure 2).

The interplay between magnetohydrodynamic and general relativistic effects was explored by Shibata et al. (2007), finding that if poloidal fields and differential rotation are present, the magnetorotational instability drives turbulence that transports angular momentum and heats the disk. Due to the MHD algorithm employed, these models also require a floor of density $\sim 10^6 \text{ g cm}^{-3}$, which again prevents the development of viscously driven winds out to large radius. The effect of gray radiation transport has been investigated by Shibata & Sekiguchi (2012), and general relativistic simulations of tori formed in BH-NS mergers have recently been reported by Deaton et al. (2013).

Lee et al. (2005) evolved tori over timescales up to a few 100 ms, using initial conditions from a merger simulation. They used a smoothed particle hydrodynamics method, and included a realistic equation of state, neutrino optical depth corrections, and the effect of nuclear recombination in the energetics of the disk. In contrast to our models, they assumed that the electron fraction satisfies beta equilibrium, parameterized the NSE abundances by the analytic relation of Qian & Woosley (1996), included all components of the viscous stress tensor, and focused on relatively massive tori. Lee et al. (2009) extended the evolution to a few seconds, considered a pseudo-Newtonian potential, and explored a wide range of tori masses and viscosity parameters. They found that the accretion rate drops sharply at late times as a consequence of including the recombination energy of alpha particles, an effect that we reproduce in our models (c.f. Figure 1).

The properties of the disk evolution and outflows found here are in qualitative agreement with the 1D model of MPQ09. MPQ09 predicted a somewhat larger mass of unbound material, and a distribution of electron fraction extending to higher values $Y_e \gtrsim 0.3$. In hindsight, this discrepancy can be understood by the fact that MPQ09 counted all mass in the disk outside the point of Y_e freeze-out as eventually becoming unbound, whereas our calculations show that only the outer edge of the disk (where Y_e is lowest) achieves sufficiently high energy to become unbound. The temperature and density of the disk midplane in our simulations are also somewhat lower than in the 1D α -disk models of MPQ09 (they find an inner disk temperature of $\sim 10 \text{ MeV}$), resulting in less effective neutrino cooling. This discrepancy can partially be understood by the fact that α -disk models assume that viscous heating exactly balances cooling, which is not everywhere achieved in our models, leading the 1D models to overestimate the midplane density. Since radiation pressure is moderately important, lower density implies a lower temperature in vertical hydrostatic balance.

6 CONCLUSIONS

We have explored the properties of outflows generated on the viscous time by accretion disks formed in NS-NS and NS-BH mergers, with an eye on detectable electromagnetic counterparts of the gravitational wave emission and r -process nucleosynthesis. Two-dimensional, time-dependent hydrodynamic simulations with a realistic equation of

⁵ Even a neutrino luminosity as large as $L_\nu \sim 10^{53} \text{ erg s}^{-1}$ is sub-Eddington.

state, weak interactions, self-irradiation in moderately optically-thick environments, and angular momentum transport via an α -viscosity are used to characterize the driving, composition, and parameter dependencies of these outflows. Our main findings are as follows:

1. – Disks eject $\sim 10\%$ of their mass in an unbound outflow. The composition is neutron rich, with typical electron fractions $Y_e \sim 0.2$. This value arises because the ejected material comes from the outer part of the disk, which is never processed to a high equilibrium electron fraction by weak interactions. The high- Y_e material in the inner disk regions is accreted onto the BH (Fig. 6). Neutron-rich freeze-out is robust because (a) neutrino cooling regulates the disk to be mildly degenerate, which in turn regulates the equilibrium Y_e prior to the freeze-out; (b) outflows begin once the disk becomes advective and α -particles form, both which occur nearly simultaneous with freeze-out.

2. – The outflow composition is relatively robust relative to initial disk parameters (Table 1). In regions where heavy elements form ($T \sim 5 \times 10^9$ K), we obtain characteristic entropies $\sim 20 k_b$ baryon $^{-1}$ and expansion times ~ 0.1 s. The composition is not homogeneous, with spatial as well as temporal variations around the mean value (Figs. 5, 8). The expected nucleosynthetic output consists in 2nd/3rd peak r -process elements ($A \gtrsim 130$), with a small trace of He ($\sim 1\%$ by mass, but $\gtrsim 10\%$ by number), which may generate a spectroscopic signature.

3. – Small variations $\sim 10\%$ in the electron fraction are introduced by changes in the initial torus entropy and the magnitude of the viscosity. The entropy of the outflow is moderately sensitive to the initial torus mass and its initial entropy. The amount of mass ejected is sensitive only to the radius at which the torus mass resides initially. The outflow velocity is remarkably robust, with a characteristic value of $\sim 20,000$ km s $^{-1}$ at 10^9 cm.

4. – In addition to viscous heating, nuclear recombination is a fundamental component in the generation of the outflow (Fig. 1). Its exclusion results in much lower ejected masses and asymptotic velocities. We also witness the drop in the accretion rate at late times first seen by Lee et al. (2009).

5. – Self-irradiation appears to be both energetically and compositionally sub-dominant. This stems in part from the fact that irradiation is maximal around the time when the disk becomes transparent to neutrinos, which for most of our low-mass disks corresponds to early times in the disk evolution. The subsequent drop in disk temperatures and densities lowers both the amount of neutrinos emitted and their mean energies (Fig. [3]), diminishing the relative importance of neutrino energy deposition as time passes. The effects of self-irradiation become noticeable only when completely removing optical depth corrections (Fig. 7). Even then, changes in global quantities are only of the order of 10%.

There are many possible improvements to the model. Self-consistent angular momentum transport by magnetohy-

drodynamic turbulence, magnetocentrifugal winds, and/or self-gravity (for more massive disks) would yield a first-principles estimate on the spatial distribution of angular momentum and heating in the disk. A full general-relativistic code would help address whether the properties of the inner disk are important, particularly regarding neutrino self-irradiation with rapidly spinning black holes. More realistic initial conditions would shed light on whether the initial angular momentum distribution is of consequence for the timing and asymptotic properties of the ejecta. The possible effects of late ‘fall-back’ accretion of tidal tail material (e.g. Metzger et al. 2010) on the disk evolution and outflows, should also be explored. More accurate neutrino physics and three-dimensional modeling would be needed if precise predictions for the outflow properties are necessary.

A more detailed analysis of the nucleosynthesis products and electromagnetic signal generated by these outflows will be carried out in subsequent work.

ACKNOWLEDGMENTS

We thank Stephan Rosswog, Thomas Janka, Almudena Arcones, Gabriel Martínez, Will East, Andrei Beloborodov, Tony Piro, Eliot Quatert, Dan Kasen, and Luke Roberts for stimulating discussions and/or comments on the manuscript. We also thank the anonymous referee for helpful comments that improved the manuscript. RF is supported by NSF grant number AST-0807444. BDM acknowledges support from Columbia University. The software used in this work was in part developed by the DOE NNSA-ASC OASCR Flash Center at the University of Chicago. Computations were performed at the IAS *Aurora* cluster.

APPENDIX A: ACCRETION RATE FOR OPAQUENESS TO NEUTRINOS

Here we provide an analytic derivation of the critical accretion rate \dot{M}_{opaque} above which the inner disk becomes opaque to neutrinos. A steady-state disk is optically thick at radii interior to the point at which the vertical optical depth to neutrino absorption obeys

$$\tau_\nu \equiv \Sigma \kappa_\nu / 2 > 1, \quad (\text{A1})$$

where Σ is the disk surface density and κ_ν is the mean opacity. For an accretion disk in steady-state, the accretion rate and surface density are related by $\dot{M} = 3\pi\nu\Sigma$ at radii much greater than the inner boundary, where $\nu = \alpha c_s H$ is the kinematic viscosity; c_s is the sound speed; $H = c_s / \Omega_K$ is the disk scaleheight; and $\Omega_K = (GM_{\text{BH}}/r^3)^{1/2}$ is the Keplerian orbital frequency. At accretion rates $\dot{M} \gtrsim \dot{M}_{\text{ign}}$, the inner disk is neutrino-cooled, such that the midplane is sufficiently dense that gas pressure exceeds radiation pressure, and the opacity is dominated by the absorption of neutrinos on free nuclei (CB07). In this case $c_s \simeq (4k_B T / 3m_p)^{1/2}$ and $\kappa_\nu \simeq \kappa_0 T^2$ (where $\kappa_0 \simeq 4.5 \times 10^{-39}$ K $^{-2}$ cm 2 g $^{-1}$; e.g. Di Matteo et al. 2002). Equation (A1) can thus be expressed as a condition on the accretion rate

$$\dot{M} > \frac{8\pi\alpha k_B}{\kappa_0 m_p \Omega_K T} \quad (\text{A2})$$

Now, for an optically thin disk, the midplane temperature is determined by the balance between viscous heating $\dot{q}_{\text{visc}} = (9/4)\nu\Omega_K^2$ and neutrino cooling $\dot{q}_\nu \simeq \dot{q}_{\nu,0}T^6$ (due to e^-/e^+ captures on free nuclei, where $\dot{q}_{\nu,0} \simeq 8 \times 10^{-43} \text{T}^6 \text{ erg s}^{-1} \text{g}^{-1} \text{K}^{-6}$), viz.

$$T \simeq 1.25(\alpha k_B/m_p)^{1/5} \Omega_K^{1/5} \dot{q}_{\nu,0}^{-1/5} \quad (\text{A3})$$

$$\approx 5.9 \times 10^{10} \text{ K} \left(\frac{\alpha}{0.03}\right)^{1/5} \left(\frac{M_{\text{BH}}}{3M_\odot}\right)^{-1/5} \left(\frac{r}{R_g}\right)^{-3/10}, \quad (\text{A4})$$

where we have now expressed radius in terms of gravitational radii $R_g = GM_{\text{BH}}/c^2$. Substituting equation (A4) into equation (A2), we find

$$\dot{M} > 2 \times 10^{-3} M_\odot \text{ s}^{-1} \left(\frac{\alpha}{0.03}\right)^{4/5} \left(\frac{M_{\text{BH}}}{3M_\odot}\right)^{7/10} \left(\frac{r}{R_g}\right)^{9/5} \quad (\text{A5})$$

Now, since most of the total neutrino luminosity is released from radii just outside the innermost stable circular orbit R_{isco} , we can evaluate equation (A5) at $r \approx 2R_{\text{isco}}$ to define a critical accretion rate

$$\dot{M}_{\text{opaque}} \simeq 0.15 M_\odot \text{ s}^{-1} \left(\frac{\alpha}{0.03}\right)^{4/5} \left(\frac{M_{\text{BH}}}{3M_\odot}\right)^{7/10} \left(\frac{R_{\text{isco}}}{6R_g}\right)^{9/5} \quad (\text{A6})$$

above which the majority of the radiated energy will originate from an optically-thick environment. This expression agrees reasonably well with CB07, who find that for $\alpha = 0.1$, $\dot{M}_{\text{opaque}} = 0.7M_\odot \text{ s}^{-1}$ and $0.06M_\odot \text{ s}^{-1}$ for a BH of spin $a = 0$ ($R_{\text{isco}} = 6R_g$) and $a = 0.95$ ($R_{\text{isco}} \simeq 1.5R_g$), respectively, although the dependence on α that they find, $\dot{M}_{\text{opaque}} \propto \alpha$ is slightly different than than the $\propto \alpha^{4/5}$ dependence that we find in equation (A6).

APPENDIX B: SELF-IRRADIATION AND WEAK INTERACTIONS

The implementation of charged-current weak interaction and self-irradiation follows closely that of Fernández (2012) in the context of core-collapse supernovae, with suitable modifications to account for the disk geometry. We consider only electron-type neutrinos and antineutrinos, with emission and absorption rates following Bruenn (1985).

Our prescription for self-irradiation assumes that neutrinos are emitted from a ring of material at a radius R_{em} . This approximation is motivated by the fact that the neutrino emissivity displays a single peak inside the disk, where most of the emission is generated. Figure B1 illustrates the shape of the function for model S-def. We choose the emission radius to be an average weighted by the neutrino emissivity (eq. [16]). This location coincides within $\sim 10\%$ with the radius inside which 50% of the neutrino emission is generated.

Each fluid element on the ring is assumed to emit isotropically, with a total luminosity equal to the instantaneous volume integral of the emissivities, and with an energy spectrum following a Fermi-Dirac distribution with zero chemical potential. The number density of neutrino species i per unit energy ϵ , propagation direction \hat{k} , and angular position on the ring ϕ' is

$$\frac{\partial^3 n_{\nu_i}}{\partial \phi' \partial \cos \theta_k \partial \epsilon} = \frac{2\pi}{(hc)^3} f_{\nu_i}(\epsilon, T_{\nu_i}, L_{\nu_i}; r, \theta)$$

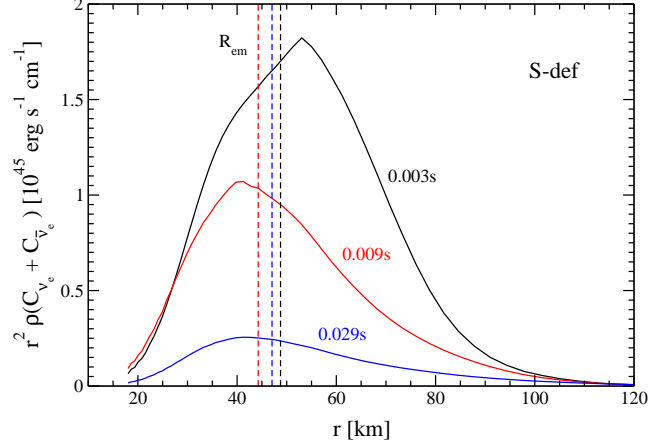


Figure B1. Snapshots of the angle-integrated neutrino emissivity for model S-def. Times shown correspond to orbits 1 (black), 3 (red), and 10 (blue) at $r = R_0$. The vertical dashed line shows the location of R_{em} (eq. [16]) in each of the models.

$$= \frac{2\pi}{(hc)^3} \frac{L_{\nu_i}/2\pi}{(7/16)4\pi\mathcal{R}^2\sigma_{\text{SB}}T_{\nu_i}^4} \times F_{\text{FD}}(\epsilon, T_{\nu_i}, 0) \Theta(\cos \theta_k - \cos \theta_{k,\text{min}}) \quad (\text{B1})$$

where θ_k is the angle between the propagation vector and the radial direction, and Θ is the step function. The intensity is assumed to be azimuthally symmetric around the propagation direction. The Fermi-Dirac function is given by

$$F_{\text{FD}}(\epsilon, T, \mu) = \frac{1}{e^{(\epsilon-\mu)/kT} + 1}, \quad (\text{B2})$$

and the minimum angle between \mathbf{k} and the radial direction is

$$\cos \theta_{k,\text{min}} \simeq 1 - \frac{1}{2} \left(\frac{\mathcal{R}}{D}\right)^2 \quad (\text{B3})$$

to lowest order in \mathcal{R}/D , where \mathcal{R} is the radius of a spherical emitting element in the ring, and

$$D(r, \theta, R_{\text{em}}, \phi') = r \left[1 + \left(\frac{R_{\text{em}}}{r}\right)^2 - 2\frac{R_{\text{em}}}{r} \sin \theta \cos \phi' \right]^{1/2} \quad (\text{B4})$$

is the distance to a point in the disk with coordinates (r, θ) from the emitting blob in the ring, as depicted in Figure B2. Keeping the lowest order terms arising from equation (B3) ensures that \mathcal{R} scales out of the problem. By using equation (B4) to capture the global geometry of the problem, we are ignoring light bending and Doppler effects.

The rates per baryon of production and destruction of electrons and positrons that enter equation (14) are given respectively by

$$\Gamma_{e^-} = \frac{2\pi m_{\text{n}} c}{(hc)^3 \rho} \left[\int d\phi' \int d\cos \theta_k \int \epsilon^2 d\epsilon (\kappa_{\nu_e} + j_{\nu_e}) f_{\nu_e} - \int d\cos \theta_k \int \epsilon^2 d\epsilon j_{\nu_e} \right] \quad (\text{B5})$$

$$\Gamma_{e^+} = \frac{2\pi m_{\text{n}} c}{(hc)^3 \rho} \left[\int d\phi' \int d\cos \theta_k \int \epsilon^2 d\epsilon (\kappa_{\bar{\nu}_e} + j_{\bar{\nu}_e}) f_{\bar{\nu}_e} \right]$$

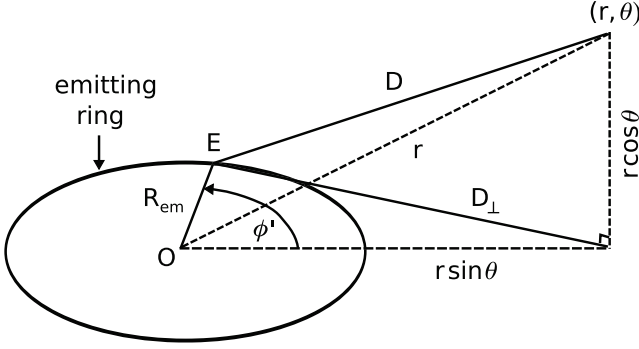


Figure B2. Geometry for self-irradiation. All of the neutrino luminosity is assumed to originate in a ring on the midplane with radius R_{em} . A point in the disk with coordinates (r, θ) lies at a distance D from an emitting element E with azimuthal angle ϕ' . The total emission received by the point in the disk is a sum over the emission from each ring element, leading to an angular dependence I_{ang} (eq. [B15], Figure B3).

$$- \int d \cos \theta_k \int \epsilon^2 d \epsilon j_{\bar{\nu}_e} \quad (\text{B6})$$

where j_{ν_i} and κ_{ν_i} are the emissivity and absorption coefficient, respectively, associated with electron-type neutrinos or antineutrinos (as subscripted). The coefficients are given by (Bruenn 1985)

$$j_{\nu_e}(\epsilon, T, \mu_e, n_p) = \frac{\tilde{G}_F^2}{\pi} (g_V^2 + 3g_A^2) n_p F_{\text{FD}}(\epsilon, T, \mu_e) \times [\epsilon + \Delta_m]^2 \left[1 - \frac{m_e^2 c^4}{(\epsilon + \Delta_m)^2} \right]^{1/2} \quad (\text{B7})$$

$$j_{\bar{\nu}_e}(\epsilon, T, \mu_e, n_p) = \frac{\tilde{G}_F^2}{\pi} (g_V^2 + 3g_A^2) n_n \times F_{\text{FD}}(\epsilon - \Delta_m, T, -\mu_e) \times [\epsilon - \Delta_m]^2 \left[1 - \frac{m_e^2 c^4}{(\epsilon - \Delta_m)^2} \right]^{1/2} \times \Theta(\epsilon - \Delta_m - m_e c^2) \quad (\text{B8})$$

$$\kappa_{\nu_e}(\epsilon, T, \mu_e, n_p) = \frac{\tilde{G}_F^2}{\pi} (g_V^2 + 3g_A^2) n_n [1 - F_{\text{FD}}(\epsilon, T, \mu_e)] \times [\epsilon + \Delta_m]^2 \left[1 - \frac{m_e^2 c^4}{(\epsilon + \Delta_m)^2} \right]^{1/2} \quad (\text{B9})$$

$$\kappa_{\bar{\nu}_e}(\epsilon, T, \mu_e, n_p) = \frac{\tilde{G}_F^2}{\pi} (g_V^2 + 3g_A^2) n_p \times [1 - F_{\text{FD}}(\epsilon - \Delta_m, T, -\mu_e)] \times [\epsilon - \Delta_m]^2 \left[1 - \frac{m_e^2 c^4}{(\epsilon - \Delta_m)^2} \right]^{1/2} \times \Theta(\epsilon - \Delta_m - m_e c^2), \quad (\text{B10})$$

where μ_e is the chemical potential of electrons, n_n and n_p the number density of free neutrons and protons, respectively, $\tilde{G}_F = G_F/(\hbar c)^3$ the Fermi constant, g_V and g_A the vector and axial coupling constants, respectively, and $\Delta_m = (m_n - m_p)c^2$ the difference between the rest mass energy of neutrons and protons.

The energy source terms that enter equation (15) are

$$\mathcal{H}_{\nu_e} = \frac{2\pi m_n c}{(hc)^3 \rho} \int d\phi' \int d \cos \theta_k \int \epsilon^3 d \epsilon [j_{\nu_e} + \kappa_{\nu_e}] f_{\nu_e} \quad (\text{B11})$$

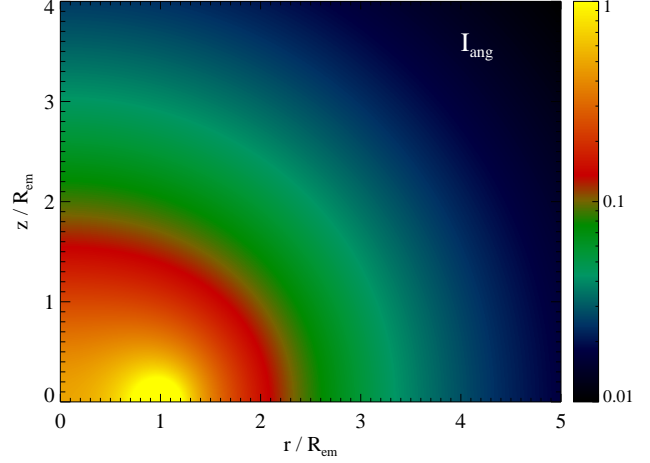


Figure B3. Angular dependence of the radiation field (eq. [B15]). The angular factor approaches a pure inverse square law at large distances from the origin (eq. [B16]).

$$\mathcal{H}_{\bar{\nu}_e} = \frac{2\pi m_n c}{(hc)^3 \rho} \int d\phi' \int d \cos \theta_k \int \epsilon^3 d \epsilon [j_{\bar{\nu}_e} + \kappa_{\bar{\nu}_e}] f_{\bar{\nu}_e} \quad (\text{B12})$$

$$\mathcal{C}_{\nu_e} = \frac{4\pi m_n c}{(hc)^3 \rho} \int \epsilon^3 d \epsilon j_{\nu_e} \quad (\text{B13})$$

$$\mathcal{C}_{\bar{\nu}_e} = \frac{4\pi m_n c}{(hc)^3 \rho} \int \epsilon^3 d \epsilon j_{\bar{\nu}_e}. \quad (\text{B14})$$

The anisotropy of the global radiation field decouples from the energy integrals, and enters through a dimensionless prefactor

$$I_{\text{ang}} = \frac{1}{2\pi} \left(\frac{R_{\text{em}}}{r} \right)^2 \int_0^{2\pi} \frac{d\phi'}{2 [D(r, \theta, R_{\text{em}}, \phi')/r]^2} \quad (\text{B15})$$

$$\simeq \frac{1}{2} \left(\frac{R_{\text{em}}}{r} \right)^2 \left[1 - \left(\frac{R_{\text{em}}}{r} \right)^2 \right] + \frac{1}{2\pi} \left(\frac{R_{\text{em}}}{r} \right)^4 \sin^2 \theta \quad (\text{B16})$$

in all terms containing an f_{ν_i} factor (D is given by eq. [B4]). The spatial dependence of I_{ang} is shown in Figure B3. In the inner regions of the disk, this function varies by factors of order unity following the annular geometry of the emission region. It becomes increasingly spherical for larger radii. Quantitatively, this can be seen from equation (B16), which is a series expansion in R_{em}/r . Due to the azimuthal averaging, the leading error term scales like the 4th power of this ratio. The integral diverges when $r = R_{\text{em}}$. To avoid excessive heating by artificial concentration of the emission at this radius, and given that the spatial distribution of the emission has a finite width (Figure B1), we impose $I_{\text{ang}} \leq 1$. The effect of this upper limit can also be seen in Figure B3.

All terms containing a f_{ν_i} factor are also multiplied by a normalization constant N_{ν_i}

$$N_{\nu_i} = \frac{L_{\nu_i}}{(7/16)4\pi R_{\text{em}}^2 \sigma_{\text{SB}} T_V^4}, \quad (\text{B17})$$

which ensures that the incident flux is consistent with the total neutrino luminosity L_{ν_i} emitted by the disk. The denominator normalizes the assumed Fermi-Dirac spectrum in

f_{ν_i} . The neutrino temperature used is the same for both neutrino species, and is equal to the average, mass-weighted gas temperature in an (angle integrated) annular region centered on R_{em} , with a radial width of 10%. This averaging is performed to smooth over stochastic fluctuations in localized disk regions.

Weak rates are tabulated as a function of the gas temperature T , electron degeneracy parameter including rest mass $\mu_e/(k_B T)$, and neutrino temperature T_ν . The angular function I_{ang} is also tabulated in cylindrical coordinates, covering the range $(r/R_{\text{em}}) \in [0, 10]$. Outside of this range, the asymptotic expansion in equation (B16) is used.

APPENDIX C: HEAVY ELEMENT NUCLEOSYNTHESIS

Here we review the conditions for nucleosynthesis of heavy elements in hot outflows, such as those from binary NS merger accretion disks. Free nuclei recombine into α -particles once the temperature decreases to $T \lesssim 10^{10}$ K, the energy from which plays a key role in powering the disk outflows explored in this paper. Heavier elements start to form once the temperature decreases further, $T \lesssim 5 \times 10^9$ K, such that the reaction ${}^4\text{He}(\alpha n, \gamma){}^9\text{Be}(\alpha n){}^{12}\text{C}$ occurs (at higher temperatures, the abundance of ${}^9\text{Be}$ is limited by photodisintegration).

Immediately after ${}^{12}\text{C}$ forms, multiple additional α -captures produce heavy ‘seed’ nuclei with characteristic mass $\bar{A} \simeq 90 - 120$ and charge $\bar{Z} \simeq 35$ (the ‘ α -process’; Woosley & Hoffman 1992). Whether nucleosynthesis proceeds to even heavier r -process nuclei depends primarily on the ratio of free neutrons to seed nuclei once the α -process completes. Since the formation of ${}^{12}\text{C}$ is the rate limiting step in forming seeds, the quantity and distribution of r -nuclei synthesized depends on the entropy S , electron fraction Y_e , and expansion timescale t_{exp} at the radius where $T \simeq 5 \times 10^9$ K.

If the electron fraction of the outflow is less than that of the seed nuclei themselves, i.e. $Y_e \lesssim \frac{\bar{Z}}{\bar{A}} \simeq 0.3$, then the ${}^4\text{He}(\alpha n, \gamma){}^9\text{Be}(\alpha n){}^{12}\text{C}$ reaction is ultimately limited by the total number of α -particles (the neutron abundance can be considered fixed for purposes of calculating the ${}^{12}\text{C}$ reaction yield). In this case the final mass fraction of alpha particles is approximately given by (Hoffman et al. 1997)

$$X_{\text{He}} = [(2Y_e)^{-2} + \mathcal{F}]^{-1/2}, \quad (\text{C1})$$

where

$$\mathcal{F} = 1.8 \times 10^4 (1 - 2Y_e) \left(\frac{\bar{Z}}{36} \right) \left(\frac{t_{\text{exp}}}{0.1 \text{ s}} \right) \left(\frac{S}{20 k_B \text{ nuc}^{-1}} \right)^{-3}, \quad (\text{C2})$$

where \mathcal{F} is proportional to the reaction rate for ${}^4\text{He} \rightarrow {}^{12}\text{C}$ integrated over the timescale available for burning $\sim t_{\text{exp}}$. The reaction rate depends on S^{-3} since $\rho \propto 1/S$ at fixed temperature, and since ${}^4\text{He}(\alpha n, \gamma){}^9\text{Be}(\alpha n){}^{12}\text{C}$ is an effective four-body reaction. Any mass not trapped in α -particles ends up in r -process nuclei with mass fraction

$$X_r = 1 - X_{\text{He}}, \quad (\text{C3})$$

and mass number greater than

$$A = \bar{A} \left(1 - \frac{1 - 2Y_e}{X_r} \right)^{-1}. \quad (\text{C4})$$

If $\mathcal{F} \ll 1$ then very little ${}^{12}\text{C}$ forms (‘He-rich freeze-out’), in which case helium achieves its maximum abundance $X_{\text{He}} = 2Y_e$, unchanged from its value just after α recombination. Since most of the available protons are trapped in ${}^4\text{He}$, the r -process nuclei produced in this case are very massive, easily reaching beyond the third peak $A \gtrsim 195$ (and likely undergoing fission). Even if $\mathcal{F} = \infty$ ($X_r = 1$), however, nucleosynthesis will still reach the Lanthanide elements ($A \gtrsim 139 = A_{\text{La}}$) if the outflow is sufficiently neutron-rich: $Y_e \lesssim \frac{\bar{A}}{2A_{\text{La}}} \approx 0.30 - 0.40$. Thus, given the low electron fraction of the disk outflows that we find in §4.2 ($\bar{Y}_e \approx 0.2$), we expect Lanthanides to easily form, resulting in a high optical opacity (Kasen et al. 2013).

REFERENCES

- Abadie J., Abbott B. P., Abbott R., Abbott T. D., Abernathy M., Accadia T., Acernese F., Adams C., Adhikari R., Affeldt C., et al. 2012, *Phys. Rev. D*, 85, 122007
- Abadie J., Abbott B. P., Abbott R., Abernathy M., Accadia T., Acernese F., Adams C., Adhikari R., Ajith P., Allen B., et al. 2010, *Classical and Quantum Gravity*, 27, 173001
- Abramovici A., Althouse W. E., Drever R. W. P., Gursel Y., Kawamura S., Raab F. J., Shoemaker D., Sievers L., Spero R. E., Thorne K. S., 1992, *Science*, 256, 325
- Acernese F., et al., 2009, *Classical and Quantum Gravity*, 26, 085009
- Ajith P., Babak S., Chen Y., Hewitson M., Krishnan B., Whelan J. T., Brüggmann B., Diener P., et al., 2007, *Classical and Quantum Gravity*, 24, 689
- Audi G., Wapstra A. H., Thibault C., 2003, *Nuclear Physics A*, 729, 337
- Barnes J., Kasen D., 2013, *ApJ*, submitted, arXiv:1303.5787
- Bartos I., Brady P., Marka S., 2012, *ArXiv e-prints*
- Bauswein A., Goriely S., Janka H.-T., 2013, *ApJ*, submitted, arXiv:1302.6530
- Bauswein A., Janka H.-T., Hebel K., Schwenk A., 2012, *Phys. Rev. D*, 86, 063001
- Beloborodov A. M., 2003, *ApJ*, 588, 931
- Beloborodov A. M., 2008, in Axelsson M., ed., *American Institute of Physics Conference Series Vol. 1054 of American Institute of Physics Conference Series, Hyper-accreting black holes*. pp 51–70
- Bloom J. S., et al., 2009, *ArXiv e-prints*
- Bruenn S. W., 1985, *ApJS*, 58, 771
- Caron B., Derome L., Flaminio R., Grave X., Marion F., Mours B., Verkindt D., Cavalier F., Viceré A., 1999, *Astroparticle Physics*, 10, 369
- Chawla S., Anderson M., Besselman M., Lehner L., Liebling S. L., Motl P. M., Neilsen D., 2010, *Physical Review Letters*, 105, 111101
- Chen H.-Y., Holz D. E., 2012, *ArXiv e-prints*
- Chen W.-X., Beloborodov A. M., 2007, *ApJ*, 657, 383
- Colella P., Woodward P. R., 1984, *JCP*, 54, 174
- Cornish N., Sampson L., Yunes N., Pretorius F., 2011, *Phys. Rev. D*, 84, 062003
- Darbha S., Metzger B. D., Quataert E., Kasen D., Nugent P., Thomas R., 2010, *MNRAS*, 409, 846

- Deaton M. B., Duez M. D., Foucart F., O'Connor E., Ott C. D., Kidder L. E., Muhlberger C. D., Scheel M. A., Szilagyi B., 2013, arXiv:1304.3384
- Dessart L., Hillier D. J., Li C., Woosley S., 2012, MNRAS, 424, 2139
- Dessart L., Ott C. D., Burrows A., Rosswog S., Livne E., 2009, ApJ, 690, 1681
- Di Matteo T., Perna R., Narayan R., 2002, ApJ, 579, 706
- Dubey A., Antypas K., Ganapathy M. K., Reid L. B., Riley K., Sheeler D., Siegel A., Weide K., 2009, J. Par. Comp., 35, 512
- Duez M. D., Foucart F., Kidder L. E., Ott C. D., Teukolsky S. A., 2010, Classical and Quantum Gravity, 27, 114106
- East W. E., Pretorius F., Stephens B. C., 2012, Phys. Rev. D, 85, 124009
- Eichler D., Livio M., Piran T., Schramm D. N., 1989, Nature, 340, 126
- Faber J. A., Baumgarte T. W., Shapiro S. L., Taniguchi K., Rasio F. A., 2006, Phys. Rev. D, 73, 024012
- Faber J. A., Grandclément P., Rasio F. A., Taniguchi K., 2002, Physical Review Letters, 89, 231102
- Faber J. A., Rasio F. A., 2012, Living Reviews in Relativity, 15, 8
- Fairhurst S., 2009, New Journal of Physics, 11, 123006
- Fernández R., 2012, ApJ, 749, 142
- Fernández R., Metzger B. D., 2013, ApJ, 763, 108
- Foucart F., 2012, PRD, 86, 124007
- Foucart F., Duez M. D., Kidder L. E., Scheel M. A., Szilagyi B., Teukolsky S. A., 2012, Phys. Rev. D, 85, 044015
- Foucart F., Duez M. D., Kidder L. E., Teukolsky S. A., 2011, Phys. Rev. D, 83, 024005
- Freiburghaus C., Rosswog S., Thielemann F., 1999, ApJ, 525, L121
- Goriely S., Bauswein A., Janka H.-T., 2011, ApJ, 738, L32
- Hawley J. F., 2000, ApJ, 528, 462
- Hirose S., Krolik J. H., Stone J. M., 2006, ApJ, 640, 901
- Hoffman R. D., Woosley S. E., Qian Y.-Z., 1997, ApJ, 482, 951
- Hotokezaka K., Kiuchi K., Kyutoku K., Okawa H., Sekiguchi Y.-i., Shibata M., Taniguchi K., 2013, Phys. Rev. D, 87, 024001
- Hotokezaka K., Kyutoku K., Okawa H., Shibata M., Kiuchi K., 2011, Phys. Rev. D, 83, 124008
- Igumenshchev I. V., Abramowicz M. A., 1999, MNRAS, 303, 309
- Itoh N., Hayashi H., Nishikawa A., Kohyama Y., 1996, ApJS, 102, 411
- Janka H.-T., 2001, A&A, 368, 527
- Kalogera V., Kim C., Lorimer D. R., Burgay M., D'Amico N., Possenti A., Manchester R. N., Lyne A. G., Joshi B. C., McLaughlin M. A., Kramer M., Sarkissian J. M., Camilo F., 2004, ApJL, 614, L137
- Kasen D., Badnell N. R., Barnes J., 2013, ApJ, submitted, arXiv:1303.5788
- Kizivat L.-T., Martínez-Pinedo G., Langanke K., Surman R., McLaughlin G. C., 2010, PRC, 81, 025802
- Korobkin O., Rosswog S., Arcones A., Winteler C., 2012, MNRAS, 426, 1940
- Kulkarni S. R., 2005, ArXiv Astrophysics e-prints
- Lattimer J. M., Schramm D. N., 1974, ApJ, 192, L145
- Lee W. H., Ramirez-Ruiz E., 2007, New Journal of Physics, 9, 17
- Lee W. H., Ramirez-Ruiz E., López-Cámara D., 2009, ApJ, 699, L93
- Lee W. H., Ramirez-Ruiz E., Page D., 2004, ApJ, 608, L5
- Lee W. H., Ramirez-Ruiz E., Page D., 2005, ApJ, 632, 421
- Lehner L., Palenzuela C., Liebling S. L., Thompson C., Hanna C., 2012, PRD, 86, 104035
- Li L., Paczyński B., 1998, ApJ, 507, L59
- Lucy L. B., 1991, ApJ, 383, 308
- McLaughlin G. C., Surman R., 2005, Nuclear Physics A, 758, 189
- Metzger B. D., Arcones A., Quataert E., Martínez-Pinedo G., 2010, MNRAS, 402, 2771
- Metzger B. D., Berger E., 2012, ApJ, 746, 48
- Metzger B. D., Martínez-Pinedo G., Darbha S., Quataert E., Arcones A., Kasen D., Thomas R., Nugent P., Panov I. V., Zinner N. T., 2010, MNRAS, 406, 2650
- Metzger B. D., Piro A. L., Quataert E., 2008, MNRAS, 390, 781
- Metzger B. D., Piro A. L., Quataert E., 2009a, MNRAS, 396, 304
- Metzger B. D., Piro A. L., Quataert E., 2009b, MNRAS, 396, 1659
- Metzger B. D., Thompson T. A., Quataert E., 2008, ApJ, 676, 1130
- Morrison I. A., Baumgarte T. W., Shapiro S. L., 2004, ApJ, 610, 941
- Narayan R., Piran T., Kumar P., 2001, ApJ, 557, 949
- Nissanke S., Kasliwal M., Georgieva A., 2013, ApJ, 767, 124
- Nissanke S., Sievers J., Dalal N., Holz D., 2011, ApJ, 739, 99
- O'Connor E., Ott C. D., 2011, ApJ, 730, 70
- Oechslin R., Janka H.-T., 2006, MNRAS, 368, 1489
- Paczynski B., 1986, ApJ, 308, L43
- Paczynski B., Wiita P. J., 1980, A&A, 88, 23
- Papaloizou J. C. B., Pringle J. E., 1984, MNRAS, 208, 721
- Paschalidis V., Etienne Z. B., Shapiro S. L., 2012, Phys. Rev. D, 86, 064032
- Piran T., Nakar E., Rosswog S., 2013, MNRAS, 430, 2121
- Popham R., Woosley S. E., Fryer C., 1999, ApJ, 518, 356
- Qian Y.-Z., 2000, ApJL, 534, L67
- Qian Y.-Z., Wasserburg G. J., 2007, PhysRep, 442, 237
- Qian Y.-Z., Woosley S. E., 1996, ApJ, 471, 331
- Read J. S., Markakis C., Shibata M., Uryū K., Creighton J. D. E., Friedman J. L., 2009, Phys. Rev. D, 79, 124033
- Rezzolla L., Baiotti L., Giacomazzo B., Link D., Font J. A., 2010, Classical and Quantum Gravity, 27, 114105
- Roberts L. F., Kasen D., Lee W. H., Ramirez-Ruiz E., 2011, ApJ, 736, L21+
- Rosswog S., 2005, ApJ, 634, 1202
- Rosswog S., 2012, Phil. Trans. A, in press, arXiv:1210.6549
- Rosswog S., Liebendörfer M., 2003, MNRAS, 342, 673
- Rosswog S., Liebendörfer M., Thielemann F., Davies M. B., Benz W., Piran T., 1999, A&A, 341, 499
- Rosswog S., Piran T., Nakar E., 2013, MNRAS, 430, 2585
- Ruffert M., Janka H.-T., 1999, A&A, 344, 573
- Ruffert M., Janka H.-T., Schaefer G., 1996, A&A, 311, 532
- Setiawan S., Ruffert M., Janka H.-T., 2004, MNRAS, 352, 753
- Setiawan S., Ruffert M., Janka H.-T., 2006, A&A, 458, 553
- Shakura N. I., Sunyaev R. A., 1973, A&A, 24, 337
- Shibata M., 2005, Physical Review Letters, 94, 201101

- Shibata M., Sekiguchi Y., 2012, *Progress of Theoretical Physics*, 127, 535
- Shibata M., Sekiguchi Y.-I., Takahashi R., 2007, *Progress of Theoretical Physics*, 118, 257
- Stephens B. C., East W. E., Pretorius F., 2011, *ApJL*, 737, L5
- Stone J. M., Pringle J. E., Begelman M. C., 1999, *MNRAS*, 310, 1002
- Surman R., McLaughlin G. C., Ruffert M., Janka H.-T., Hix W. R., 2008, *ApJ*, 679, L117
- Tanaka M., Hotokezaka K., 2013, *ApJ*, submitted, arXiv:1306.3742
- Timmes F. X., Swesty F. D., 2000, *ApJS*, 126, 501
- Uryū K. ō., Shibata M., Eriguchi Y., 2000, *Phys. Rev. D*, 62, 104015
- van der Sluys M., Raymond V., Mandel I., Röver C., Christensen N., Kalogera V., Meyer R., Vecchio A., 2008, *Classical and Quantum Gravity*, 25, 184011
- Wanajo S., Janka H.-T., 2012, *ApJ*, 746, 180
- Wen L., Chen Y., 2010, *Phys. Rev. D*, 81, 082001
- Woosley S. E., Hoffman R. D., 1992, *ApJ*, 395, 202